Fall 12-2022

Prediction of Meltpool Depth in Laser Powder Bed Fusion Using In-Process Sensor Data, Part-Level Thermal Simulations, and Machine Learning

Grant King
University of Nebraska-Lincoln, gking@huskers.unl.edu

King, Grant, "Prediction of Meltpool Depth in Laser Powder Bed Fusion Using In-Process Sensor Data, Part-Level Thermal Simulations, and Machine Learning" (2022). *Mechanical (and Materials) Engineering -- Dissertations, Theses, and Student Research*. 186.
https://digitalcommons.unl.edu/mechengdiss/186

PREDICTION OF MELTPOOL DEPTH IN LASER POWDER BED FUSION USING IN-PROCESS SENSOR DATA, PART-LEVEL THERMAL SIMULATIONS, AND MACHINE LEARNING

by

Grant Alan Maxwell King

A THESIS

Presented to the Faculty of
The Graduate College at the University of Nebraska
In Partial Fulfillment of Requirements
For the Degree of Master of Science

Major: Mechanical Engineering & Applied Mechanics

Under the Supervision of Professor Jeffrey Shield
& Professor Prahalada Rao
Lincoln, Nebraska
December 2022

PREDICTION OF MELTPOOL DEPTH IN LASER POWDER BED FUSION USING IN-PROCESS SENSOR DATA, PART-LEVEL THERMAL SIMULATIONS, AND MACHINE LEARNING

Grant Alan Maxwell King, M.S.

University of Nebraska, 2022

Advisors: Jeffrey Shield and Prahalada Rao

The goal of this thesis is the prevention of flaw formation in laser powder bed fusion additive manufacturing process. As a step towards this goal, the objective of this work is to predict meltpool depth as a function of in-process sensor data, part-level thermal simulations, and machine learning. As motivated in NASA's Marshall Space Flight Center specification 3716, prediction of meltpool depth is important because: (1) it can serve as a surrogate to estimate process status without the need for expensive post-process characterization, and (2) the meltpool depth provides an avenue for rapid qualification of microstructure evolution. To achieve the aforementioned objective, twenty-one Inconel 718 samples were designed and built with a variety of processing parameters ranging from a power of 200 W to 370 W and a scan speed of 670 mm/s to 1250 mm/s. These parts were characterized and the meltpool depth was measured through optical microscopy. A combination of part-level thermal simulations from a spectral graph theory method and in-process sensor data from infrared thermal camera and a meltpool imaging pyrometer were used as inputs to simple machine learning models to predict the meltpool depth. The meltpool depth was correctly predicted with an accuracy of F-Score 85.9%. This exploratory work provided an avenue for rapid prediction of microstructure evolution in metal additive manufacturing.

Acknowledgements

Foremost, I would like to thank my thesis advisors Dr. Shield of the Mechanical and Materials Engineering department at the University of Nebraska-Lincoln, and Dr. Rao of the Industrial and Systems Engineering department at Virginia Polytechnic Institute and State University. Dr. Shield has been a constant supporter of my education for my entire educational career. His support over the years and especially in the last few months as I finished my research, has made completion of my masters possible. I would also like to thank Dr. Rao. His support has allowed me opportunities and experiences that I would not have had otherwise. His support and guidance made the completion of this work possible. In addition, I would like to thank thesis committee member Dr. Cole for his valuable input to improve the quality of this work.

I would like to acknowledge the help and support of Ajay Krishnan, from Edison Welding Institute (EWI), for his help and expertise in additive manufacturing. I would also like to thank Alexander Riensche and Nicholas Piercy for their collaboration in creation of various parts of the experiment and programs used in this work and for their knowledge in graph theory thermal simulations. I would like to give a special thanks to Benjamin Bevans for his assistance and encouragement throughout my time at UNL and away. He has been a foundation for my understanding of machine learning, a source of guidance, and a sounding board for the many ideas and directions my research has taken during my time at the University of Nebraska.

Lastly, I would like to thank my family and significant others for their support and encouragement, not only in the completion of this work but also all through life. I would especially like to thank my parents, Robert and Kim King and my sister, Sydney Lardy for their guidance, unyielding support, and confidence in me throughout my life.

Funding and Industry Acknowledgements

I would like to thank the National Science Foundation (NSF) for supporting this work. This M.S. thesis was funded by the NSF via the following grants:

OIA-1929172:

RII Track-4: Understanding the Fundamental Thermal Physics in Metal Additive Manufacturing and its Influence on Part Microstructure and Distortion.

CMMI-1752069:

CAREER: Smart Additive Manufacturing - Fundamental Research in Sensing, Data Science, and Modeling Toward Zero Part Defects.

ECCS-2020246:

AI Institute: Planning: AI-Enabled Secure and Responsive Smart Manufacturing

PFI-TT 2044710:

PFI-TT: Ultrafast Thermal Simulation of Metal Additive Manufacturing

CMMI-1920245:

MRI: Acquisition of an X-Ray Computed Tomography System at the University of Nebraska-Lincoln for Advancing Multidisciplinary Research and Education in the Great Plains Region

I would also like to thank and acknowledge Edison Welding Institute for their support of my work and for the use of their facilities.

Table of Contents

List of Figures

List of Tables

CHAPTER 1 – INTRODUCTION

1.1 Background and Motivation

This thesis aims to show prediction of meltpool depth in laser powder bed fusion (LPBF) using in-process sensor data, part-level thermal simulations, and machine learning. LPBF is an additive manufacturing (AM) process that uses a laser beam to selectively melt powder layer-by-layer to manufacture a part. This is done by having a thin layer of powder raked or rolled across a build plate (substrate); the laser then selectively melts the powder. This powder solidifies and the process is repeated with a new layer of powder raked or rolled across a build plane [1]. Figure 1-1 shows a representation of the LPBF process where powder is stored in the powder reservoir until it is needed to coat the build plane in powder. The reservoir is raised and the recoater pushes or rakes the powder into the build area where the laser can sinter the powder [2]. The laser is typically focused by using a special lens called the F-theta lens. This lens maintains a fixed focal length no matter what angle the laser beam strikes the powder [3]. With the powder melted and the newest layer complete, the build plate is then moved down by a set layer height; this keeps the build plane consistent. This set distance is most commonly 20 μm to 100 μm [4]–[8]. Typically in the LPBF process, the laser power ranges from 200 W to 500 W, and the laser scan speed is in the range of 500 $\mathrm{mm \cdot s^{-1}}$ to 1000 $\mathrm{mm \cdot s^{-1}}$ [4].

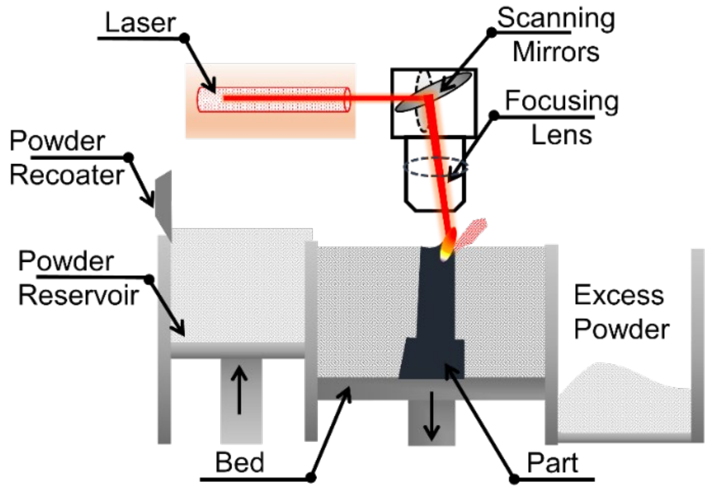

Figure 1-1: Representation of the laser powder bed fusion process where a laser is focused onto a build plane and powder is melted. The build plate then moved downward and the powder reservoir upwards. A recoater then rakes the powder over the build plane and the laser melts this new layer; this process repeats until the part is complete.

Meltpool depth and microstructure from LPBF manufactured parts are highly dependent on the thermal history of the part during material deposition [9], [10]. Currently characterization of the microstructure must be completed post-processing. There are a variety of ways to characterize AM parts, however, a scanning electron microscope (SEM) is a typical tool used to investigate microstructural characteristics. These high-resolution, small field of view images captured using SEM can be used to explore the grain growth of the part [5], [8]. For a larger field of view, optical microscopy is conducted, and this provides data related to the meltpool depth.

If this measurable meltpool depth can be predicted in-situ using sensor data, then undesirable meltpool depths and resultant microstructures could be detected and measured without the need for expensive post-process characterization. In this thesis, a combination of part-level thermal simulations and in-process sensor data (infrared thermal camera and meltpool imaging pyrometer) is used as inputs to machine learning models to predict the meltpool depth of a part.

1.2 Objectives

The goal of this is to understand the relationship between process parameters, meltpool characteristics and meltpool depth. To achieve this goal the following two objectives of this work were performed:

1. predicting meltpool depth using in-process sensing and thermal information; and
2. exploring the relationship between primary dendritic arm spacing and thermal history.

To achieve the first objective, samples were designed and built with a variety of processing parameters and subsequently characterized. These parts were confirmed to be devoid of porosity up to an accuracy of 16 µm voxels through the use of X-ray computed tomography (XCT). The meltpool depth was found through optical measurements. An in-process optical imaging setup was developed to allow for the analysis of the build and to extract meltpool information, such as shape or thermals of the build. Additionally, a layer-by-layer thermal simulation of the LPBF process was performed. The high-dimensional data generated from the sensors and thermal model were converted to a low-dimensional data set via the use of physics-informed feature extraction. This low-dimensional feature set was then used for training and testing machine learning models for the prediction of meltpool depth.

To address the second objective, scanning electron microscopy was performed to extract images of all twenty-one parts. Subsequently primary dendritic arm spacing was measured from the extracted images. The primary dendritic arm spacing was analyzed and compared to the thermal history from both sensor and model data. For this work only a visual analysis of this data was done. This initial work lays out the methodology that is needed to extract useful information from in-process sensor data and thermal simulations and demonstrates that it is possible to predict meltpool depth. With this work and methodology, future works such as prediction of primary dendritic arm spacing, may be performed by future researchers.

1.3 Organization of the Thesis

The organization of this thesis is as follows: A brief summary of the relevant literature looking into the need for meltpool depth prediction and in-situ sensing and monitoring in LPBF is described in Chapter 2. This is followed by a description of the experimental studies, with sections on the LPBF machine used, the sensors used, the machine schematics, the design of the build plate and parameter study, and NASA meltpool depth standard in Chapter 3. Chapter 4 describes the methodology for preparation of the parts, classification of meltpool depths, how primary dendritic arm spacing was measured, how features were extracted, and a review of machine learning models. The results of this work are presented in Chapter 5, where the features that were extracted were used as inputs into machine learning models. Chapter 6 summarizes the conclusions of this work and future research directions.

CHAPTER 2 – LITERATURE REVIEW

2.1 The Need for Meltpool Depth Prediction

The laser powder bed fusion process has immense potential and is one of the most popular manufacturing methods of metals in additive manufacturing [11]. However it has current limitations to overcome. Representative examples of current limitations are material constraints, surface finish, part accuracy, and repeatability [12]. Measuring meltpool depth is crucial because it helps manufacturers and researchers understand an AM machine's resistance to variation. NASA uses meltpool depth as a tool for machine qualification to show the repeatability of the machine across builds. NASA states that these meltpool characteristics are indicative of the health of the process and robustness to variations [13]. Another reason that the meltpool depth is important is the control of the meltpool regime. If the meltpool is too shallow there could be lack of fusion and if there is over penetration, keyholing can occur, both of which lead to increased porosity [14]. In order to grow LPBF in terms of reliability and control of the process, meltpool depth must be a quantifiable control metric. Using trial and error to obtain consistent and controllable meltpool structure, there could be hundreds of builds that end in failure. There are over 100 parameters that could influence the reliability and quality of a part [9], [15]. To address this concern of part inconsistency, meltpool depth was chosen as a metric to predict.

Some outstanding issues with nickel-based alloys are discussed in an article by Attallah *et al.* [16] where the properties and the effect of the AM process on the formation of the microstructure are discussed. This paper investigates issues of LPBF AM products such as microstructure anisotropy, defect formation mechanisms, process optimization, and residual stress development. Columnar grain structure is generally expected from the AM process; this microstructure usually results in grains that grow in the direction of the heat flux (*i.e.,* downward toward the substrate or build plate). Due to the repeated heating and cooling of a part in the AM process there is heterogeneity on the micron scale that can be seen as the “fish-scale-like” meltpool morphology. This article states that there is still future work that needs to be done to address residual stress evolution, control of microstructure growth, and process optimization [16].

An article by Sagar Patel *et al.* [14] explores the melting modes in LPBF by looking at two operational regimes, conduction and keyhole. These regimes affect melting and create differences in microstructure and thus mechanical properties. The author goes on to state that the importance of prediction and control of meltpool geometry comes from the need to control microstructure heterogeneity. The geometry of the meltpool (width, depth, and length of the meltpool) can impact part density from different effects such as lack of fusion, unstable keyhole melting, and layer delamination or crack formation due to thermal stresses. Creation of tools to identify printing regimes build a strong basis for understanding defects and optimization of the LPBF AM process and lead to the customization and tailoring of material properties in AM [14].

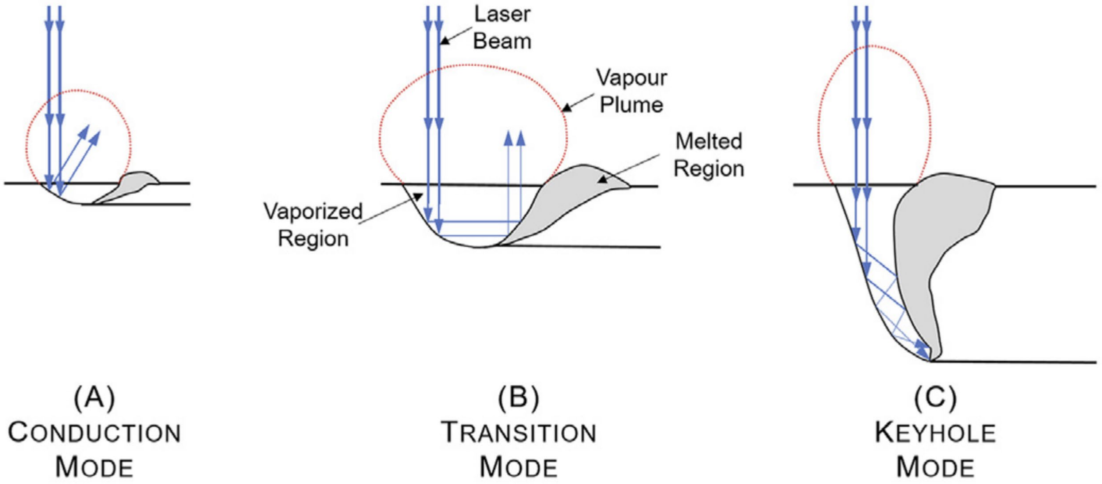

Figure 2-1: Illustration of (A) conduction, (B) transition, and (C) keyhole regimes. The laser beam refracts and bounces off the powder and material. In the conduction regime this is stable and does not create porosity. In the keyhole regime there is deeper penetration that is caused by multiple reflections of the laser that can create and then trap vapor causing porosity [14].

While the parts in this thesis do not stray into the keyhole regime, the article by Patel shows the value of being able to predict this regime. This is because the keyhole regime has a direct relationship to meltpool depth and by extension, the prediction of the meltpool depth [14], [17], [18]. With proper prediction of meltpool depth using in-situ sensing, customized parameters can be created on a layer-by-layer basis to generate customized builds.

There has been significant research to explore the meltpool and its effect on the resultant part quality in LPBF. The focus has been to detect defects and then eliminate them through process parameter optimization [19]–[21]. Many of these papers use single tracks of the laser, such as Vecchiato *et al*. [22]; in this work the meltpool microstructure and morphology from single laser exposures were studied. Through the study of depositing

316L stainless steel using a pulsed laser, the influence of inputted energy density on meltpool morphology, microstructure, and temperature fields was analyzed. Here the authors found that laser exposure time was found to influence the meltpool depth; they found an increase of meltpool depth from 50 μm to 300 μm as the laser exposure increased [22]. With this it can be understood that there is a relationship between process parameters and the meltpool depth.

A study on the prediction of meltpool behavior was done by Reynolds in his doctoral dissertation [23]. The author endeavored to predict the meltpool behavior in LPBF using a high-fidelity model. To control the meltpool process, the energy distribution delivered to the meltpool was explored. Through the use of an optimization process framework, via an inverse solution method to solve the heat of the meltpool, a model of the single-track laser parameter conditions was created to avoid defects. This work shows that optimal surface temperatures can be used as a control mechanism to avoid LPBF defects such as lack of fusion and keyhole [23].

In a work by Qilin Guo *et al.* [24], the characterization and quantification of meltpool variation under constant input energy density was studied. This was done by using in-situ high-speed, high-energy x-ray imaging of the meltpool. The dimensions of the meltpool were measured, and the results show that the meltpool dimensions exhibited an increasing trend as the laser power and laser scan speed also increased. This work also shows that there is a relationship between the length/width ratio and length/depth ratio. This is to say that the shape of the meltpool from the top down is related to the depth of the meltpool. This work shows that the meltpool has a preference towards increasing depth rather than expanding in the transverse direction when the laser power and laser scan speed are simultaneously increased [24]. This shows that there is a connection between process parameters, meltpool shape, and meltpool depth. This connection is the basis for what inputs could be needed to predict meltpool depth using machine learning.

Gustavo Tapia *et al.* [25] created a process that uses a Gaussian process-based surrogate model of the LPBF process that predicts meltpool depth in single-track experiments. This was done as a statical framework that considers power and scan speed to determine the regimes of the process whether that be conduction or keyhole regimes [25]. While this method had great results, it is limited to a single track of the laser. This research does not show the complexities that come with a fully built part. This work was done as a single track atop the build plate. This is where the highest heat transfer can occur as the build plate is a large mass of material; it acts as a heatsink pulling much of the heat away. A part that has extended farther above the build plate has more opportunities to accumulate heat, subsequently limiting the amount of heat being pulled away. This heat accumulation is not present in these works and could have an impact on the meltpool depth.

Gaikwad *et al.* [26] developed a machine learning model for the prediction of track width. This was done for Single tracks of 316L stainless steel. The machine learning-based predictive models were used with pyrometer and high-speed video camera data collected under a wide range of laser power and laser velocity settings. This work incorporates the knowledge from known physical processes into a machine learning framework. The pyrometer measures were taken in-situ of the meltpool, which consisted of thermal temporal characteristics. High-speed video signatures were used to measure the shape characteristics of the meltpool. With their features extracted, multiple machine learning frameworks were applied and trained to predict the width of the single-track segment. It was found that their best preforming model was a sequential decision analysis neural network (SeDANN) model with an R^2 of 0.87 or 87% [26]. This work shows that it is possible to create a successful machine learning model that can take in features from sensors, using a sparse feature set in the prediction of a physical meltpool characteristic.

Gaikwad *et al.* [27] used sensor data to create a machine learning model to detect laser defocusing and predict porosity type and severity. The meltpool conditions were monitored with high-speed video cameras and a temperature field imaging system. From these sensors, physically intuitive low-level meltpool signatures and characteristics were extracted. That is, from high-dimensional image-based sensor data, meltpool temperature, shape and size, and spatter intensity were extracted. Then this processed sensor data was subsequently used as input features into machine learning models. These models were trained to detect laser defocusing, porosity type, and severity. In this work multiple machine learning models were explored: multilayer perceptron (MLP), random forest (RF), support vector machine (SVM), k-nearest neighbors (KNN), and deep learning convolutional neural network (CNN). It was observed that the relatively simple SVM model had similar prediction accuracy as the more complex CNN model. The SVM and CNN have comparable results with an F-score of approximately 95% [27]. This work shows the process of meltpool data extraction and its subsequent use as features in multiple machine learning models and explores the use of sensors data being taken from its high-dimensional image-based state to low-level meltpool signature and characteristic data set for the use of machine learning.

2.2 In-situ Sensing and Monitoring in Laser Powder Bed Fusion (LPBF)

Since its creation, additive manufacturing (AM) has had large growth in industrial applications. This is due to its ability to create near net shape parts with complex geometries and create weight reduction when compared to the same contemporary parts produced by conventional manufacturing. There is a demand for these part qualities in medical and aerospace application. For these industries, these parts and the machines need to have the capability to build high quality parts with a repeatable process [28]. Even with AM's rise in capabilities, the process has not reached the same levels of reliability and repeatably in production that is seen in products of their conventionally manufactured counterparts. There is still defect formation or variation in part characteristics [4], [29]–[31]. To overcome this, there is need to implement the use of in-process sensing and monitoring. These techniques are needed to overcome the knowledge gap and aid in understanding the effect of process conditions on the resulting product, its quality, and its repeatably. In current research there are many different sensing systems designed with different goals in mind.

Montazeri *et al.* [1] developed a sensor-based monitoring system that was used to detect when there is high probability of defect formation in the LPBF process. This was done by creating a suite of sensors to monitor the thermal aspects of the meltpool and capture the meltpool shape and spatter pattern. The sensors used were a thermal camera, a photodetector, and a high-speed camera. This work describes a method for extraction of data from an image source using binarization to collect features. They used spectral graph theory approach data for the analysis of multidimensional signals and integrated this within a learning framework for prediction [1].

In Gobert *et al.* [32] work, an in-situ flaw detection system was developed that used a supervised machine learning approach that took in in-situ optical images of the LPBF process. This was done with the use of a layer-wise optical image that was processed and binary classifiers were used to predict defect and nominal condition locations. The defects were first found using X-ray computed tomography (XCT) to find defects such as cracks, porosity, or incomplete fusion. They used a machine learning model called a support vector machine (SVM) and were able to achieve classification accuracy of over 80% [32]. This work shows that there are accurate methods for taking in-process sensor data and correlating that information using machine learning to get a better understanding of the part characteristics.

Grasso and Colosimo [28] have a review of the in-situ monitoring methods in metal powder bed fusion. This review is mainly focused on the detection of defects and lays out categories of defects and their causes along with in-situ sensing equipment and set-ups. As shown in literature, there are four main meltpool-related quantities that have been measured for monitoring. They typically are the size, the shape, the temperature intensity, and the temperature profile. These characteristics of the meltpool are strongly correlated to the process parameters and the beam-material interaction [28]. Meltpool properties determine many things from the geometrical accuracy of the track and surface properties, to the porosity of the part and development of the residual stresses [33], [34]. The meltpool corresponds to the highest level of detail that is needed for in-situ monitoring of the LPBF process. The sensing of the meltpool must be done with high fidelity as the meltpool makes up a very small region in the micron scale. Along with the high spatial resolution that is needed, there is also a need for a very high sampling rate. For laser powder bed fusion, the sample rate must be in the order of 1,000 Hz. This work gives many different sensing systems and sensors that have been used to collect meltpool information. The two most used sensor types were pyrometry and high-speed imaging [28]. These in-process sensor systems can be used to indicate the need for active corrective actions, such as re-deposition of the powder bed or subtractive actions [28], [35]. The temperature profile is also important for the detection of things such as balling phenomena, lack-of-fusion, local over-heating and heat accumulation conditions, surface errors, and porosity formation [31], [36]. Grasso and Colosimo lay out the existing works and their sensing equipment and set-ups and discuss the use of off-axial configurations of the sensors. Off-axial sensors are not in the optical path, so the sensor gives a view of the process in a region of interest. There are many different sensors that have been used off-axial, some of which are accelerometers, ultrasound detectors, strain-gauges, thermo-couples, and x-ray detectors. From this work it is shown that the mainstream sensing methods for off-axial are typically imaging systems with infrared or optical cameras [28].

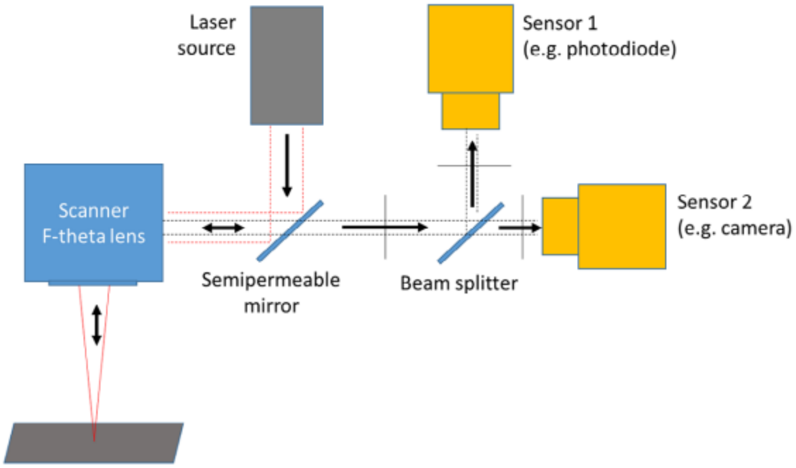

Figure 2-2: Co-axial sensing set-up for LPBF process monitoring. Sensors are able to collect data directly in line with the laser's location through the use of a semipermeable mirror and a beam splitter [28].

Co-axial sensing is when the sensor takes advantage of the way the laser in the LPBF process is directed. This is where the sensor can be set up in-line with the laser through the use of semipermeable mirrors and beam splitters, as visualized in Figure 2-2. This allows the laser strike to always be in view of the sensor. Many different sensors have been used co-axially, some of which are high-speed CMOS cameras, photodiodes, and two-wavelength pyrometers, and more [28], [37], [38].

CHAPTER 3 – EXPERIMENTAL STUDIES

The data and parts for this work were acquired at Edison Welding Institute (EWI) in Columbus, Ohio by Ajay Krishnan, Alexander Riensche, and Grant King. Ajay Krishnan is a Research Leader at EWI in the Additive Manufacturing Group. For this research, he directed Alexander Riensche and Grant King on sensor use and was the liaison for their use of EWI's Open Architecture Laser Powder Bed Fusion machine.

3.1 Edison Welding Institute Open Architecture LPBF Machine

To realize the goal of understanding and predicting meltpool depth in LPBF, experiments were done at Edison Welding Institute (EWI, Ohio). This research was performed on their Open Architecture Laser Powder Bed Fusion machine that is designed for sensor evaluation. This open architecture platform gives a base for easy integration of multiple sensors. This system also allows for the custom manipulation of process factors, such as dwell time between layers, laser power, scan speed, and scan pattern. These can be altered on a part basis and even on a layer-by-layer basis. Many commercial LPBF systems limit the control the user has over the process settings. This system's design is based on the EOS M290, which is a widely used and robust system. EWI's LPBF platform is shown in Figure 3-1.

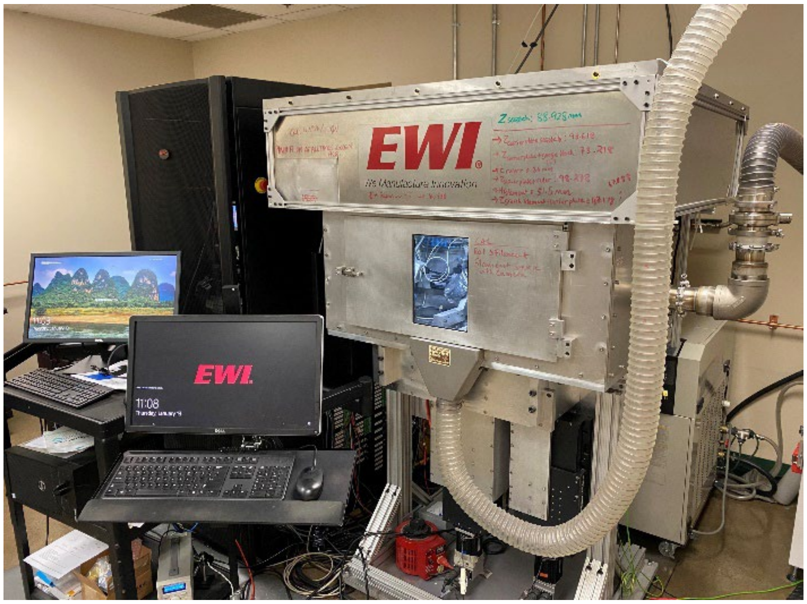

Figure 3-1: Open architecture laser powder bed fusion machine made and used at Edison Welding Institute, based on the EOS M280. This platform allows for the easy integration of multiple sensors.

EWI's machine is equipped with a 700 W Yb-fiber laser (IPG Photonics YLR – 700WC) operating in continuous mode with a wavelength of 1070 nm, a SCANLABS HurryScan20 galvanometer-mirror scanner, and a motion control system (Aerotech A3200) that is driven by CNC G-code. This G-code can be modified by the operator mid-print. The system's optics train produces a nominal spot size of 68 µm at 370 W; this was measured by an Ophir BeamWatchAM laser beam profiling system [39].

3.2 Sensors Used

Three sensors were in use on this machine, a dual wavelength pyrometer, an infrared thermal camera, and a Hall effect sensor connected to the recoater.

A Micro-Epsilon model µε thermoIMAGE TIM 640 longwave infrared (LWIR) thermal camera was mounted within the build chamber. This IR camera had a near nominal view of the build plate with a relative angle to the substrate of 80° and captured nearly the entirety of the build plate as shown in Figure 3-2.

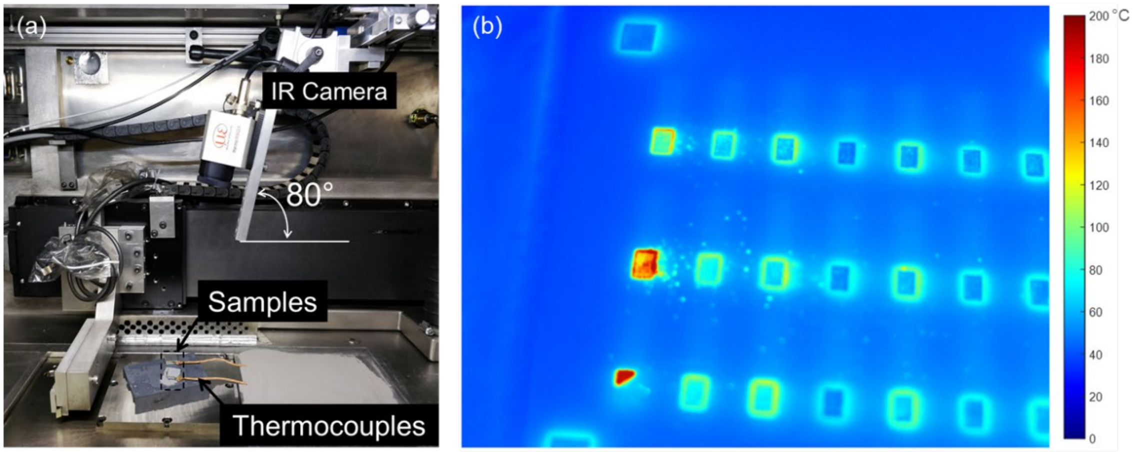

Figure 3-2: (a) Visualization of the IR camera position, along with an example of how IR calibration was performed. The IR camera was placed 80° from the substrate, allowing for a near vertical view of the process, (b) Visualization of one frame of IR data, post calibration. In this frame, 21 parts can be seen within view of the IR camera and the laser's location can be seen mid melting of a part in the lower left.

The infrared thermal data collected needed to be calibrated as it is not an absolute temperature reading but is a relative measure of the temperature. The thermal camera was calibrated post-build using a quasi-static heating technique. This approach uses a thermal mass with a known temperature measured with contact thermocouples that are then used to create a calibration curve for the IR data [40]. This was done by taking measurements of built parts that had a contact thermocouple welded to them, depicted in Figure 3-2(a). The IR temperature readings were adjusted to be absolute temperatures through a direct correlation to the temperature values recorded via the thermocouples.

Two parts were built specifically to be used post-process as sacrificial calibration blocks. These parts were two 6 mm tall cubes of Inconel 718 that were cut from the build plate, and K-type thermocouples were spot welded to the parts. These parts were placed in the build chamber atop a cartridge heater. These were then placed at the same level of the build plane as the building parts. The temperature of the heater was increased slowly, and the response (absolute) temperature of the thermocouple and the response (relative) temperature of the IR camera were recorded. To account for the different emissivity of powder and bare metal, powder was deposited on top of one of the cubes and the process was repeated and recorded. This simulates what the temperatures would be when the parts are covered in powder post recoat and when the parts are uncovered post processing.

This data from the IR camera was then correlated to the two thermocouples and a calibration curve was obtained. This was done by fitting a regression function to the recorded data under both conditions. This gives a calibration curve that can be seen in Figure 3-3. This is an industry-standard procedure and has been used in previous publications [41]–[43].

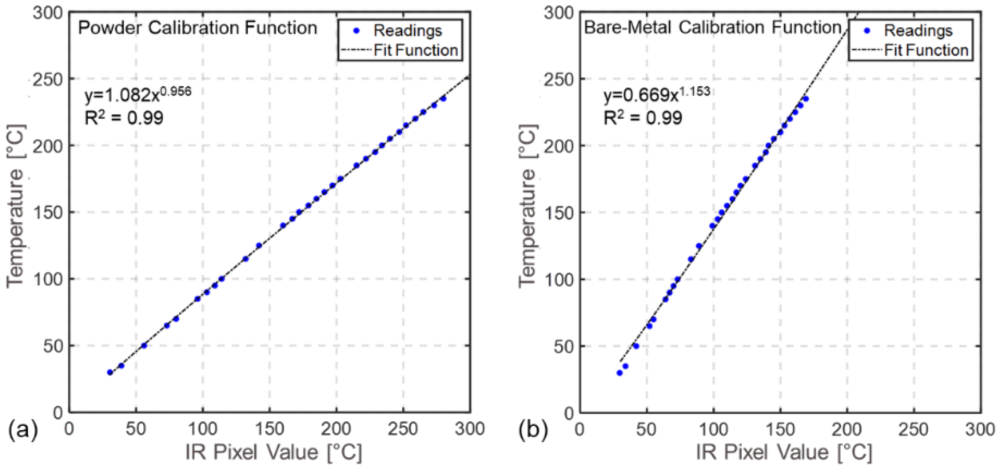

Figure 3-3: (a) Calibration curve for the infrared camera with powder on the parts and (b) with bare metal that would be seen post sintering. These calibration curves were created through the process of collecting and correlating absolute temperature data (thermocouples) to relative temperature data (infrared camera).

This calibration function has a range of 25 °C to 250 °C; this is because measurements above this range would saturate the IR camera and become inaccurate. This calibration was then applied to all the 21 parts' IR data measurements.

A two-wavelength imaging pyrometer (ThermaViz by Stratonics, Inc.), shown in Figure 3-4, was used in this work to capture the meltpool intensity and meltpool shape characteristics. This pyrometer has two high-speed cameras that capture the meltpool images at the two wavelengths, 750 nm and 900 nm. Ratio pyrometry is then used to estimate the temperature, and with calibration the measurement error is ~ 5% at 1900 K. The detailed procedure for obtaining the temperature field, with calibration of the measurements of this sensor is described in Reference [44].

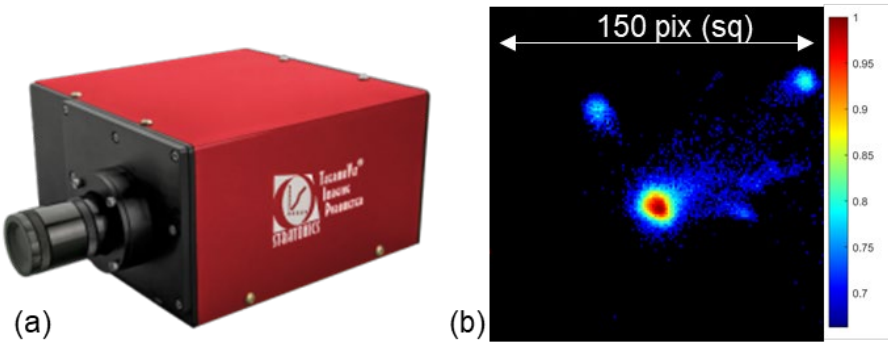

Figure 3-4: (a) Picture of the ThermaViz sensor along with (b) a representative image of a meltpool frame captured using the sensor.

The Hall effect sensor connected to the recoater measures the current being drawn by the recoater blade motors and was used to explore the recoater motion. This sensor collected current data that can be related to direct load on the sensor and the recoating time. In this work there was no impact directly related to the Hall effect sensor.

3.3 Machine Schematic

Within the build chamber, the IR camera was mounted and orientated at 80° to the build plate and captured data at a sampling rate of 1 Hz. The IR camera operates at a wavelength of 8 to 14 μm and has an optical resolution of 640 pixels × 480 pixels. The camera was given a triggering command from the G-code for starting and stopping recording of a layer, allowing for segmented data streams for each layer. The camera was mounted to capture approximately an area of 125 mm × 125 mm centered on the build plate. This gives a spatial resolution of approximately 20 pixels for mm^2. The IR camera's mounting location can be seen in Figure 3-2 and Figure 3-5.

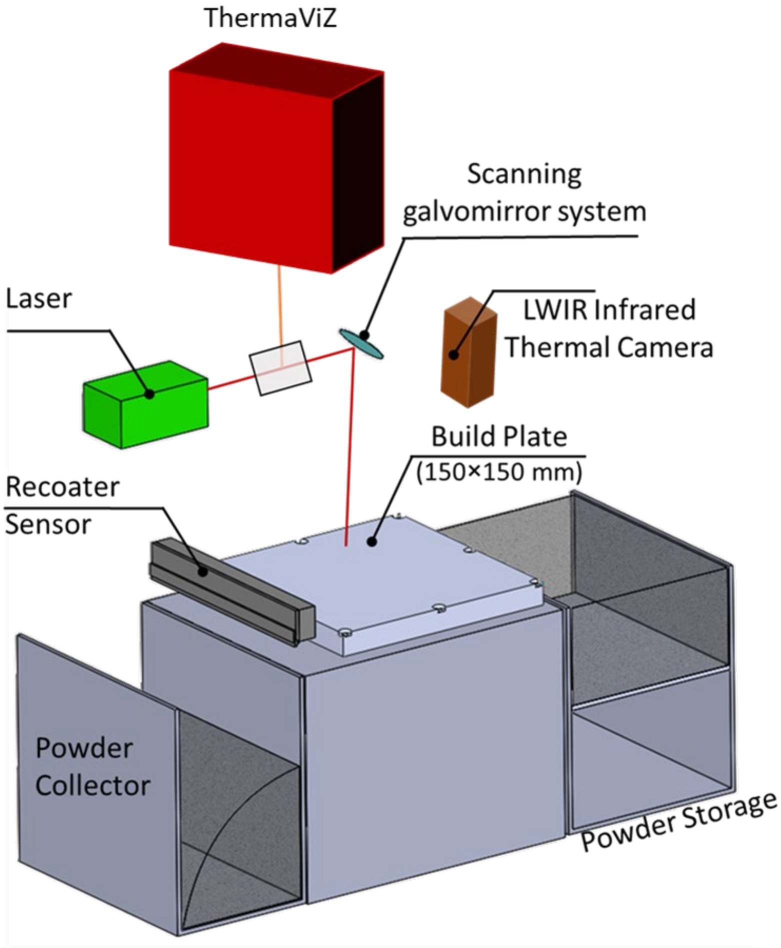

Figure 3-5: Schematic of the sensor positions in the Edison Welding Institute's open architecture machine. The infrared camera was mounted inside the build chamber, the ThermaViz sensor was mounted co-axially with the laser beam, and the recoater sensor was integrated with the machine's recoater.

For this work, there was a physical error with the ThermaViz two-wavelength pyrometer and only relative intensity and high-speed images from the camera were used. This error was from a data pin becoming faulty after shipping resulting in partial loss of camera two data. This loss of camera sync made calibration to temperature impossible. The data from camera one was still used in a normalized state. Each high-speed video image is of size 150 × 150 pixels, shown in Figure 3-4(b). This device was mounted co-axial with the laser giving a direct line of sight to the meltpool; thus the meltpool was always within view of the sensor. This was done by placing a beam splitter before the galvanometer-mirror scanner, allowing for the sensor to view the meltpool but not be damaged by the laser. The Hall effect current sensor was mounted with the recoater drive train to measure the current of the recoater drive motor.

3.4 Build Plate

This experiment was part of a set of builds that set out to explore microstructure, validate thermal simulations, and study the deformation of parts. The material that was used was Inconel 718. The parts used in this thesis were twenty-one parts of similar geometry to facilitate a design of experiments where power and scan speed settings were adjusted by ± 30% from nominal. The nominal settings are as follows: a scan velocity of (V) 960 mm/s, laser power (P) 285 W, layer thickness (T) 0.040 mm, and hatch spacing (H) 0.1 mm, this gives an applied volumetric energy density $E_V \approx 74\ \mathrm{J \cdot mm^{-3}}$ $(\frac{P}{H \times V \times T})$ and $\mathrm{P \cdot V^{-1}}$ ratio of $0.29\ \mathrm{J \cdot mm^{-1}}$. These settings were used from previous offline studies done to determine optimal settings at EWI. The set of power and velocity settings used in this work is shown in Figure 3-6.

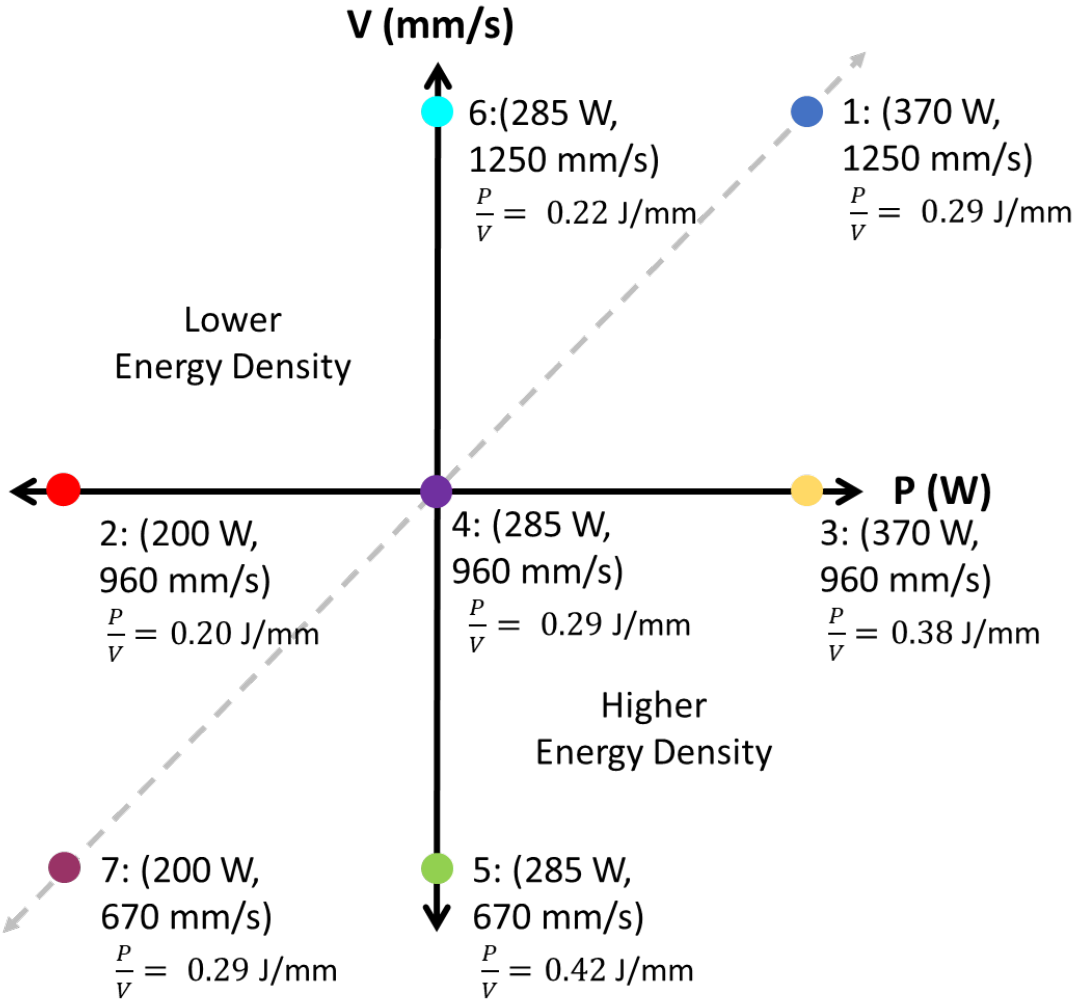

Figure 3-6: Schematic of the power and velocity changes used in this work. The x-axis depicts variation in laser power, y-axis depicts variation in laser scan speed. Nominal parameters for Inconel 718 on this machine were 285 W and 960 mm/s (4) and are found at the origin. The variation in parameters was found by adjusting power and scan speed by ± 30% from nominal. These parameters were selected to keep the meltpool within the conduction regime; the extremes that would move into the lack of fusion and keyhole regime were not used for this reason.

In addition to this parameter study of the power and scan speed, different heights of the same part geometry were explored. For this experiment, an overhang geometry was chosen for multiple reasons shown in Figure 3-7. The geometry is primarily of interest as it will accumulate heat as the part is built. This part was also chosen as it has similar shape features to the NIST Overhang Part X4 [45]. On this build plate, twenty-one overhang parts of varying heights, differing laser powers, and scan speed settings were built. The overhangs all have a base that is 5 mm x 20 mm by 6 mm tall. After this base was built, the cross-sectional area of the part was reduced due to the start of the overhang portion. There are three heights that were explored: height A - which is 20 mm tall, height B - which is 15 mm tall, and height C - which is 10 mm tall, shown in Figure 3-7. Further discussion of why these geometries were chosen can be found on page 28.

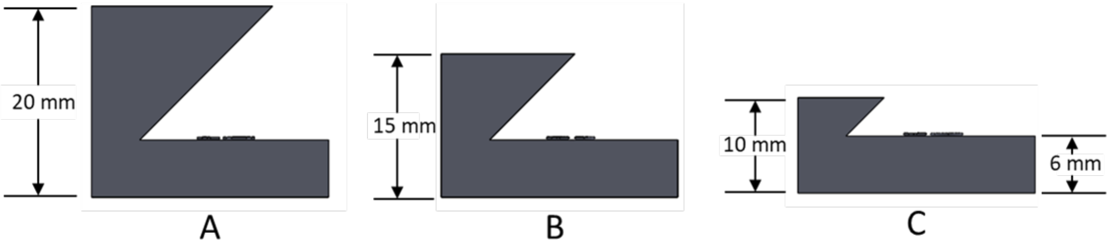

Figure 3-7: 2-D schematic of the three different heights of overhang geometries used in this work. Sample A was 20 mm, sample B was 15 mm, and sample C was 10 mm tall. These parts have similar geometries to existing National Institute of Standards and Technology process monitoring test artifact.

These parts were broken up into seven sets, each set was numbered 1 to 7. These 7 sets were then assigned a power and velocity from the parameter study schematic in Figure 3-6. The power and scan speed settings were adjusted by ± 30% from nominal. This organization of build heights and power/velocity settings is depicted in Figure 3-8(a).

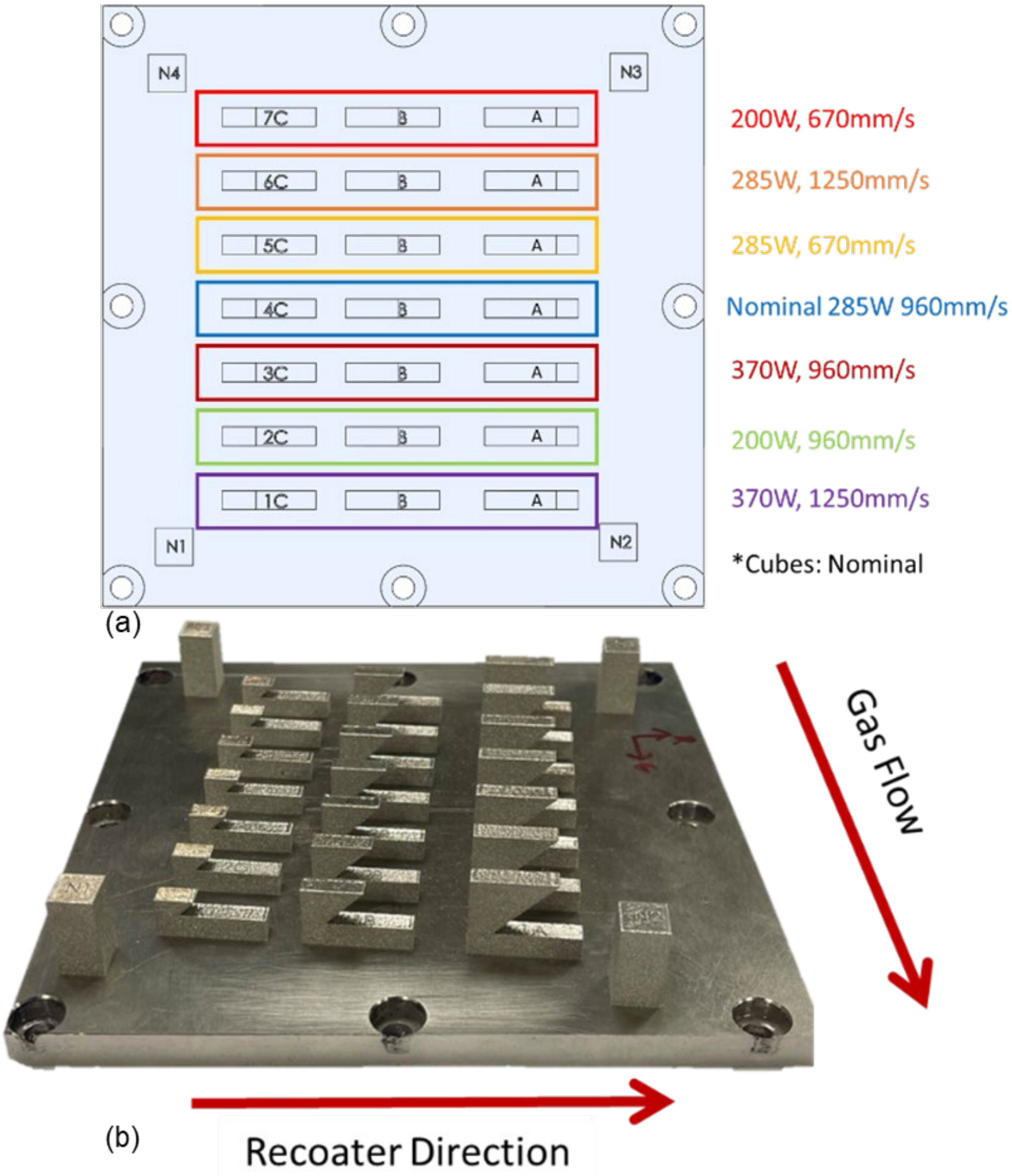

Figure 3-8: (a) Visualization of reach row of overhangs in respect to its power and velocity settings. (b) Visual of the final build plate after manufacturing.

As a full parameter study would have nine distinct settings, there were two settings that were not used. These settings were not used as the goal of the setting was to stay within the conduction regime. The first setting that was not used was 200 W and 1250 mm/s (-30% Power, + 30% Scan Speed). This was avoided as it could cause lack of fusion in the part. The lower power and faster scan speed would not allow the part to have complete bonding between successive layers. The second setting that was not used was 370 W and 670 mm/s (+ 30% Power, - 30% Scan Speed). These settings could cause keyhole porosity to occur. Keyhole porosity occurs when at the higher energy densities, the meltpool becomes unstable; the bottom of the meltpool repeatedly forms and collapses, trapping vapor in the layer. Also on this build plate were 4 cubes built at nominal settings, with a height of 20 mm that were disregarded for this work.

3.5 NASA Meltpool Depth Standard

Measuring meltpool depth is crucial because it helps manufacturers and researchers understand an AM machine's resistance to variation. NASA uses meltpool depth as a tool for machine qualification to show the repeatability of the machine across builds. NASA states that these meltpool characteristics are indicative of the health of the process and robustness to variations [13]. Another reason that the meltpool depth is important, is control of the meltpool regime. If the meltpool is too shallow, there could be lack of fusion and if there is over penetration, keyholing can occur [14].

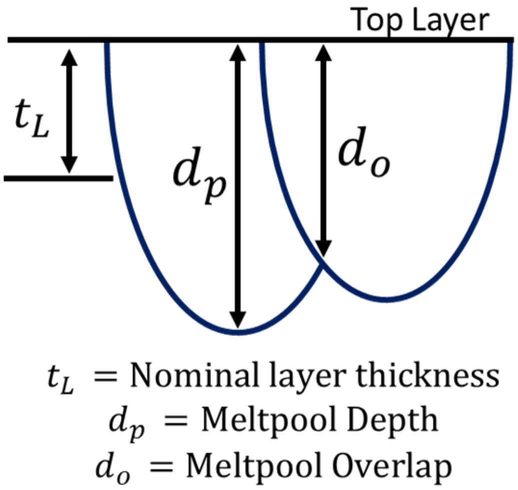

Figure 3-9: Schematic for measuring meltpool depth (d_p) and meltpool overlap (d_o). These values are measured from the topmost surface of a sample and can be normalized to the nominal layer thickness to give a layer to depth ratio. These ratios are used as a performance metric to measure repeatability of the machine across builds.

From Figure 3-9 and NASA MSFC-SPEC-3717, the technique for measurement of meltpool depth (d_p) and meltpool overlap (d_o) is described. This characterization is done using the top layer of the specimens. From the schematic given in the documentation, measurement of meltpool depth is presented as the distance from the top of the part to the lowest point on the meltpool hatch. The meltpool overlap is another metric that is used to explore the process consistency. Meltpool overlap is the distance from the top of the part to the point where a previous meltpool was intersected by the next meltpool track. For this research, the meltpool depth is explored and predicted. The ratio of meltpool depth to nominal layer thickness is used as the quantifiable tracking metric. This metric is stated in the documentation to be an average of ten or more meltpool tracks [13]. For the goal of predicting meltpool depth, the individual measurements and their normalized values were preserved to be used as the “ground truth” in machine learning models.

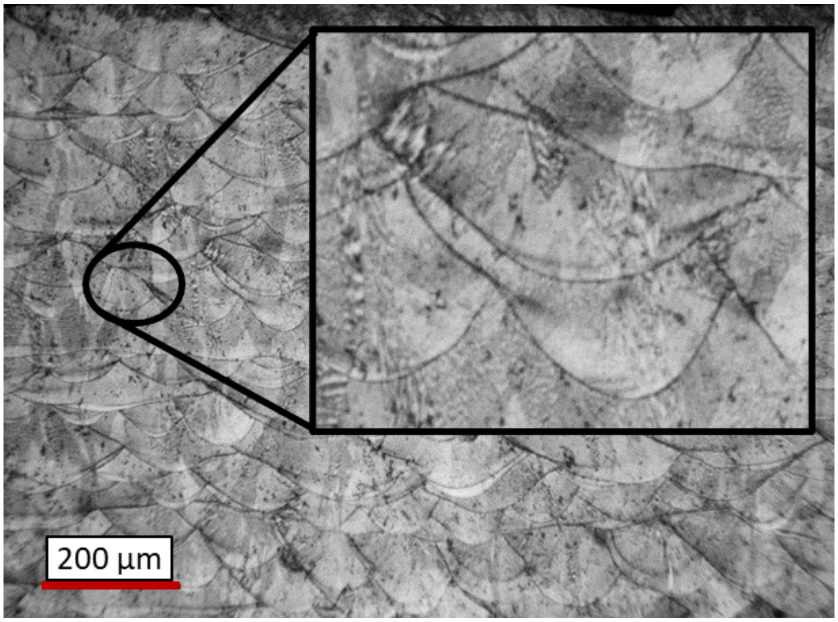

Figure 3-10: Optical image from the center of a sample shows that there is no well-defined top location from which to take measurements.

While there are other ways to quantify meltpool depth, only when measuring from the top surface (and thus the last layer) can meltpool depth be considered "absolute." When measuring the meltpool within the part, there is no way to find the top of a specific meltpool. There can only be a relative measurement to the meltpool track above, as seen in

Figure 3-10. The true top of the meltpool in the lower layers of the part have been destroyed, or written over, by new layers being deposited and sintered. Meltpool depth can only be accurately measured at the top surface.

Due to the limitation of only being able to measure the top surface meltpool depths, three different heights of the same sample geometry were printed for each parameter setting. This was done to explore the evolution of meltpool depth with height and its link to heat accumulation. The first sample, sample C, was only 10 mm tall to observe the meltpool at the start of the overhang before heat begins to accumulate. Sample B was 15 mm tall to observe the meltpool depth and half-way through the overhang when heat has moderately begun to accumulate. Finally, sample A was the full height of 20 mm to observe meltpool depth at the maximum heat accumulation. As each set of heights finish at their maximum height there will be changing in the number of parts being printed and thus the time between layers or the interlayer time. This decrease in interlayer time will also have an effect on the heat accumulation; there will be less time between the layers giving less time for cooling causing higher end-cycle temperatures. End-cycle temperatures is the temperature measured right before the next layers' laser strike; this gives the lowest temperature that the part cooled to before the start of the next layer. Further explanation of end-cycle temperatures will be discussed in section 4.4.3. This increase in heat accumulation not only from geometry but also from interlayer time will have an impact on the formation of microstructures and could have in impact on the meltpool depth. These changes in interlayer time are not inputted into the data or used as a feature set in machine learning but they are represented in the data through the end-of-cycle temperature. Where as the interlayer time decreases the general end-of-cycle temperature increases.

CHAPTER 4 – METHODOLOGY

This chapter is divided into five main sections, wherein section 4.1 the data collection of meltpool depth is discussed, section 4.2 describes the methodology for separating the meltpool depths into classification for machine learning, section 4.3 discusses the use of techniques for gathering primary dendritic arm spacing, section 4.4 describes the feature extraction from sensors simulations, with sub-sections to highlight individual sensors or methods, and section 4.5 contains a review of the machine learning models and methods with explanations of each accuracy metric and their applications.

4.1 What was Measured – Meltpool Depth

The twenty-one Inconel 718 parts were polished to 0.5 μm surface finish and then etched using an acid mixture of 170 mL of H_3PO_4, 10 mL of H_2SO_4, and 15 mL of CrO_3. These parts were imaged using an optical microscope and the acquired images were used to characterize the meltpool depth, shown in Figure 4-1.

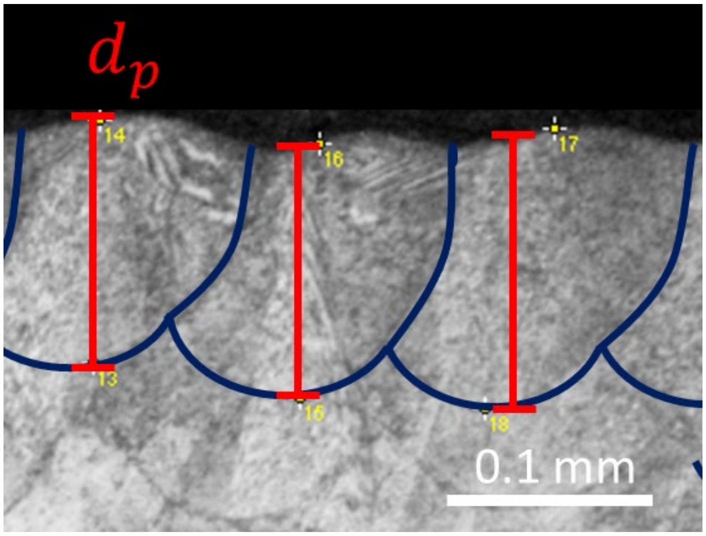

Figure 4-1: Representative example of how meltpool depth measurements were acquired. The measurements were taken from the top of the part to the bottom trough of the meltpool. This was repeated for each sample.

The top layer of the specimens was imaged completely with overlapping edges to get a complete data set of the top layer. From these images pixel locations were gathered and recorded from the top and the bottom of the meltpool tracks. While orientation of the tracks is important and connected to the total number of meltpools seen, it does not affect the measurement of depth of the meltpool. This is true because regardless of the orientation of the meltpool track relative to cross sectioning, the deepest point is visible allowing for the measurement to be taken. From a pixel measurement of the given scale bar, a ratio was found to relate the distance between locations in pixels to millimeters. Fiji was the software used to analyze the acquired optical images, which is an open-source application based on ImageJ2, an image processing software.

4.2 Classification of Meltpool Depths

For the application of classification in machine learning, the data set must be segmented into different classes or bins. These classes allow for the models to more easily predict which range of labels a new data point belongs to, as opposed to regression which aims to find an exact value. Classification and regression are discussed in more detail in section 4.5.

Three classes were created as it gives a wider range of bins to use, thus giving more applicable results than a two-class binary system. Four classes were not used as the amount of data in each class would become susceptible to bias, as the amount of data points is limited to the number of physical meltpools measured. EWI provided its goal that penetration be more than two layers. From this, it was decided that the three classes would be: Severe Under Penetration (~<1.5 layers), Poor Penetration (~1.5-2.5 layers), and Nominal Penetration (~>2.5 layers); these can be seen in Figure 4-2.

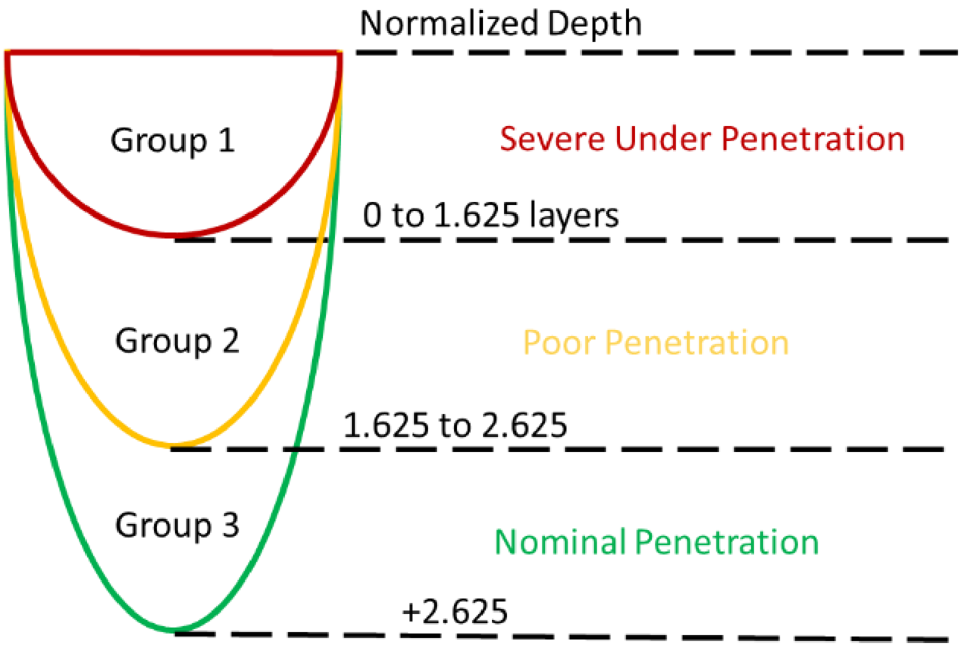

Figure 4-2: Grouping used in classification of meltpool depth. From 0 to 1.625 layers, Group 1: Severe Under Penetration, from 1.625 to 2.625 layers, Group 2: Poor Penetration, from 2.625 and up, Group 3: Nominal Penetration.

Severe under penetration occurs when the meltpool is not deep enough to remelt completely into the previous layer. This classification should warrant examination of the part and possible stopping of the print as there is risk of lack of fusion. The poor penetration class shows that there is sufficient penetration of the previous layer and no risk of lack of fusion, but meltpool depths are not reaching much past the second layer. Lastly, nominal penetration is when sufficient depth is achieved. These values also correlate to a near even split of data in each class, minimizing bias when raw data was used in the models. Further data selection is done to ensure an even split of the data classes.

4.3 Primary Dendritic Arm Spacing

The prediction of primary dendritic arm spacing (PDAS) is a complex task that is discussed further in the Future Work section. In this section, the work that has been done to collect and create the data set is discussed.

The twenty-one Inconel parts, after being etched and characterized using optical microscopy, were also examined using a scanning electron microscope (SEM). This was performed to explore and measure the PDAS.

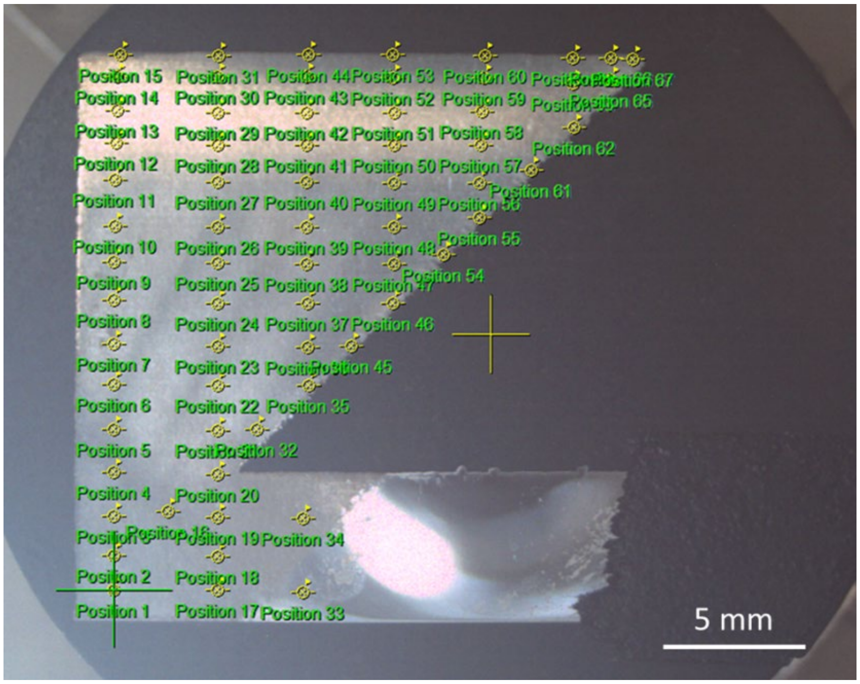

Figure 4-3: Locations on the overhang samples where SEM images were taken. At each location, two images were taken and used for PDAS analysis.

Two images were taken at 6,500x magnification at each of the positions marked on Figure 4-3. This grid-like pattern was used as it can still realistically show the evolution of the microstructure and be feasible to capture images. Figure 4-4 shows how the PDAS was measured using a bounding box. Dendrites that passed through the bounding box were used to create a cell. These cells were marked and summed. This sum was then used to divide the bounding box, giving a value, which is the Primary Dendritic Arm Spacing.

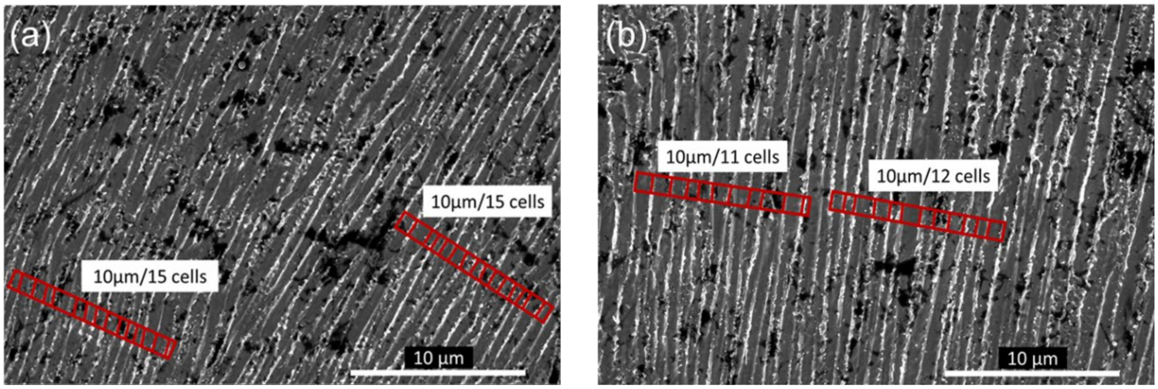

Figure 4-4: Example measurement of PDAS using 10 μm bounding box. Both images (a) and (b) were taken using SEM under 6,500x magnification, with beam accelerating voltage of 10 kV, probe current of 2 nA using a through-the-lens detector (TLD) set to detect secondary electrons (SE).

For this research, all of the cells in the two images per location were summed and the total length of the bounding boxes were used. A sample calculation can be seen below:

$$\frac{40\ [\mu\text{m}]}{15+15+11+12\ [\text{cells}]} = 0.754\ [\mu\text{m}] \tag{1}$$

From this, a map of the PDAS of the part can be created, and a data set that spans parameters and build heights can be created.

4.4 Feature Extraction

For this research, there was a total of 27 features extracted to be used in the prediction of the meltpool depth. These features are in three different groups denoting their source.

The groups are Parameters, Sensors, and Graph Theory Modeling. In this section, the extraction of these features is discussed and explored.

4.4.1 Pyrometer – Meltpool Shape Characteristics

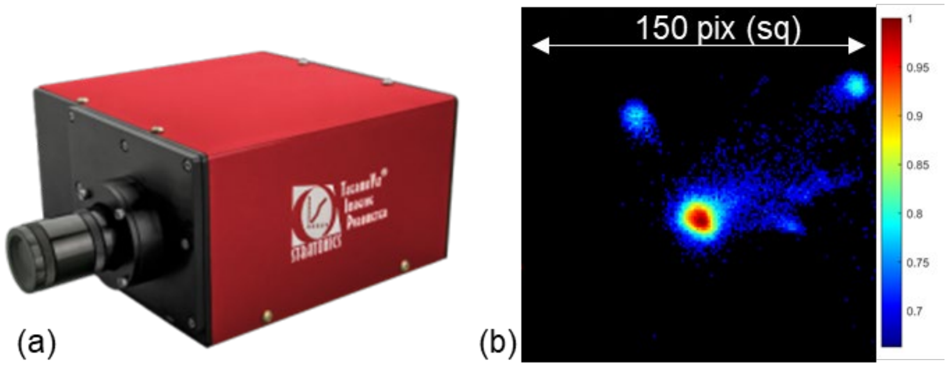

Figure 4-5: (a) Picture of the ThermaViz sensor along with (b) a representative image of a meltpool frame captured using the sensor. The intensity of the pixels was normalized to the highest intensity pixel; this was repeated for all frames and used for meltpool feature extraction.

The Stratonics ThermaViz Sensor's output is a *.vis* file that is a stream of images. These images must be processed before shape feature extraction. The raw images were first normalized to the highest intensity pixel value. This was done as there were data collection issues that prevented the temperature values from being used. From this normalized image, the meltpool was separated by applying a threshold to binarize the image. This value needs to be set at the solidus-liquidus boundary to properly separate the meltpool from its surroundings. The threshold value was found from previous work where the liquidus boundary was known. This value was normalized and found to be 0.83. From this binarized image, the shape features can be extracted using MATLAB's regionprops function. This function's output is the area, major axis, minor axis, and eccentricity, and this series of actions can be seen in Figure 4-6. The last feature extracted was the skewness of the meltpool's pixel intensity and informs the amount of heat accumulation inside of the meltpool. Area, major axis, minor axis, and eccentricity are all functions of the meltpool shape. Area is the number of pixels in the meltpool. Major and minor axes are the axes that make the ellipsoid that is the meltpool. Eccentricity is a function of the major axis and minor axis and is indicative of the circularity of an object. The eccentricity ranges from 0 to 1, with 0 indicating a perfect circle and 1 a flatter ellipse.

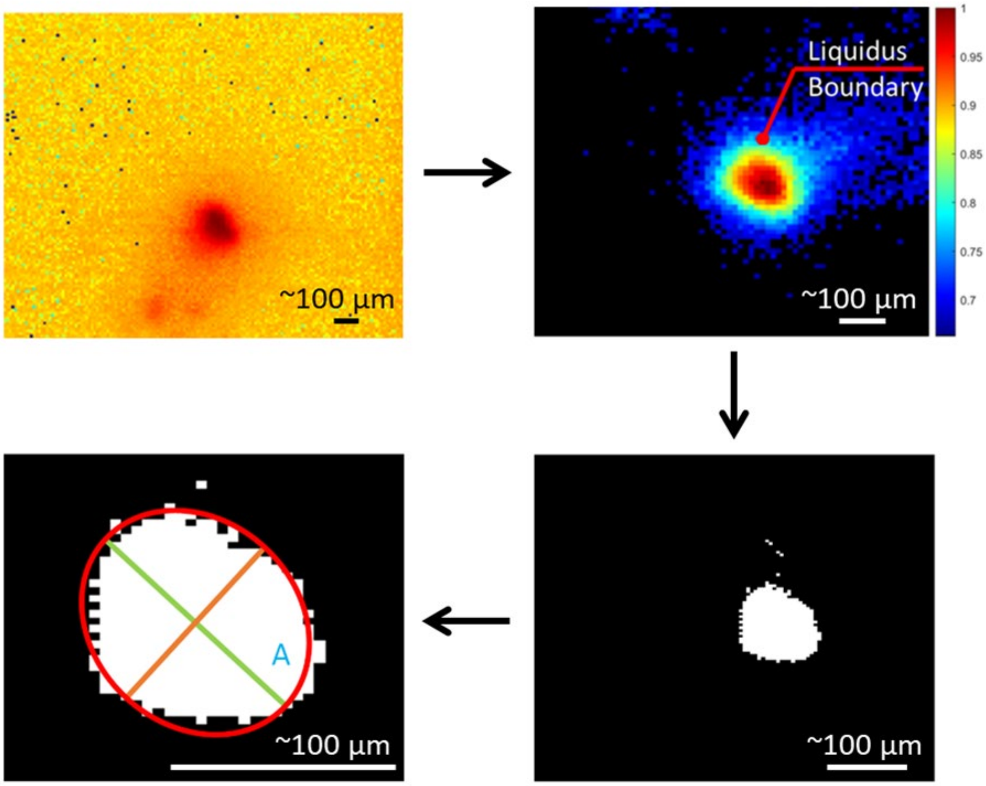

Figure 4-6: The process flow of meltpool shape extraction. Meltpool images were segmented from raw data using image filtering. Filtering was done by normalization of the pixels and then image binarization. The binarization was done using a threshold value that corresponds to the liquidus boundary. The shape features were extracted for each of these images and this process was then repeated for each frame of the pyrometer data.

4.4.2 Meltpool Data Correlation to Hatch Location

Meltpool data, which is in individual frames, needed to be matched to their corresponding location in the part. This correlation was done by finding individual hatches and evaluating which frames would belong to that hatch. This was done by using the G-code to find the spatial relationship to time. The G-code is the machine code that determines the part's shape and build parameters; this is a predetermined path that the laser takes. G-code is generated before the build and is a static set of instructions. From the part's G-code, the total distance that the laser would travel in an individual part was determined. The machine's laser has a constant velocity, this assumption is considered true because this build used sky writing to keep the hatches of the part at a constant velocity. Sky writing is when the laser is blocked or shut off at the edges of the part so that the acceleration of the turn, to start the next hatch, is not affecting the previous or the next hatch.

Knowing that the velocity is constant, the distance the laser travels and the time it takes to complete a part are proportional. As the sample rate of the sensor is known, a total number of frames can be used instead of total time, giving a part-by-part relationship for location to frame. The number of individual hatches was determined for the three different heights, and frames per hatches were used as the organizational metric. This value changed per part as each part had a different setting or scan pattern. Then the meltpool frames were organized into each hatch and averaged per hatch, giving the mean and the standard deviation of each extracted feature.

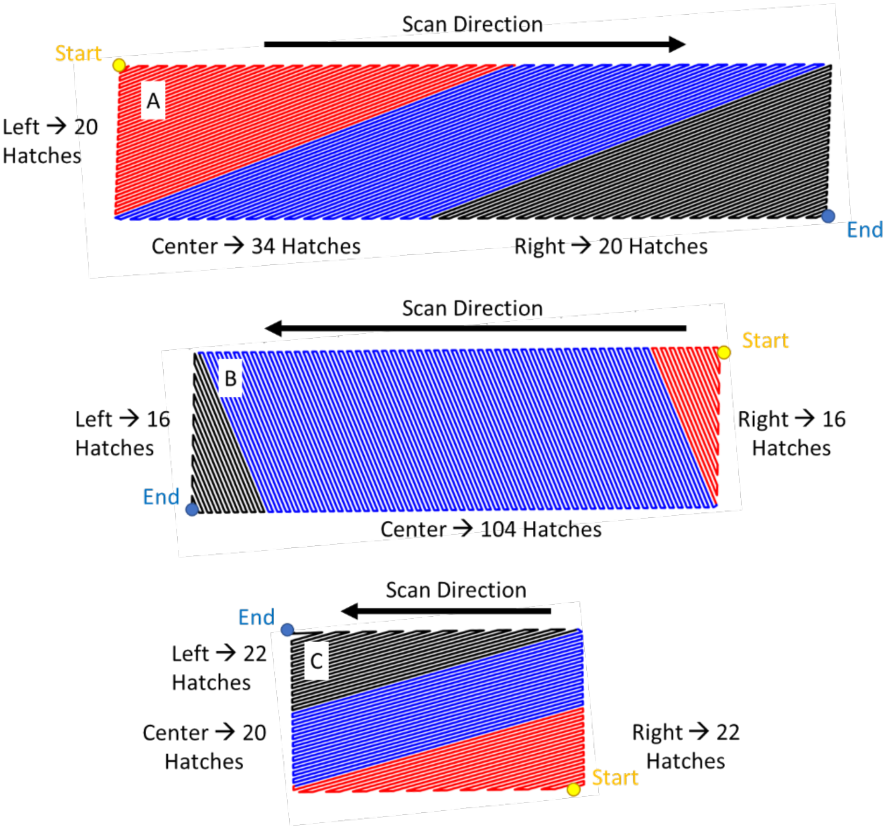

Figure 4-7: Scan pattern for the last layer of the three sample heights, A, B, and C. Patterns segmented into left, center, and right. Total length of each segment was found and used to correlate sensor frame to individual hatch in the parts. Correlated frame data was then averaged for hatch. Averaged hatch data was then associated to measured meltpool depth.

The hatches were further segmented into Left, Center, and Right hatches, shown in Figure 4-7, so the appropriate data could be applied to the meltpool depth measurements. These measurements were found by matching the number of observed meltpools to the corresponding number of G-code hatches. Using these segments in space (distance) the pyrometer frame data (time data) was sequenced to the individual measured meltpools. When there was missing data the last data point in the frame data was truncated and not correlated to a meltpool measurement. This happened when the number of meltpools was less than the number of hatches counted in the G-code. This method was chosen as the meltpools at the tip of the overhang are nonuniform or lost due to imperfection in the polishing of the part.

4.4.3 Infrared Camera - End-of-Cycle Temperature

The infrared camera was used to capture the end-of-cycle temperature (ECT) on each part on the build plate. End-of-cycle temperature is the temperature directly before the next laser strike. Extracting this data involves defining pixel location to the sample and ensuring that those locations are within the part and are updated as the part progresses in height. An area was used which was centered at these pixel locations to reduce the effect of noise in the measurement. This was a 9 x 9 pixel region where the IR values were averaged, shown by the black square in Figure 4-8, to get the raw IR temperature readings.

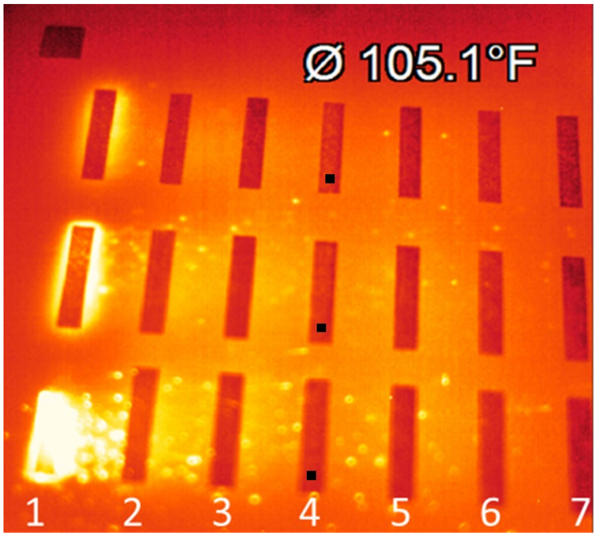

Figure 4-8: Infrared Camera view of the build plate and the seven rows of parts. Black squares depict the sampling region used for data extraction. These regions were selected for each part and the region was checked to ensure that it stayed within the area of the part as the build progressed. This data is relative temperatures that needs to be calibrated as the infrared camera captures relative intensity not absolute temperatures.

With locations selected, the heating and cooling curves were obtained and analyzed. While these heating and cooling curves are calibrated, they are not able to capture the highest temperature, as they are outside of the sensor's optical saturation range.

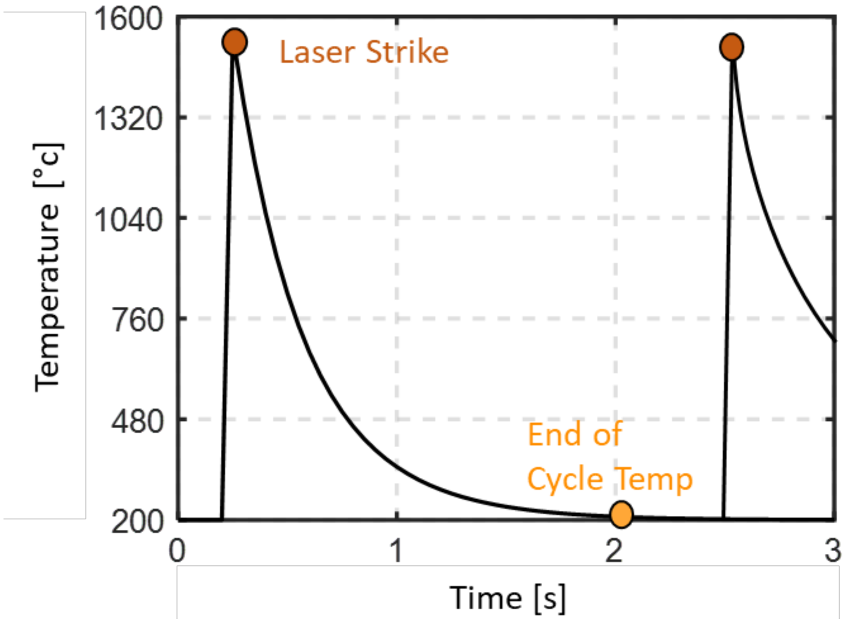

Figure 4-9: Example Schematic of two layers and end-of-cycle temperature (yellow). At laser strike there is a large increase in temperature as the material melts, after which there is a rapid cooling until the next laser strike. End-of-cycle temperature is the temperature measured just before the next laser strike.

The temperature cycle for two layers is shown in Figure 4-9. Starting with a laser strike which produces a sharp increase in temperature there is then a decrease in temperature until the next layer's laser strike. The end-of-cycle temperature is taken right before that second laser strike. For this data set, the end-of-cycle temperature is extracted from the frame before the laser strike. This process was done for all 21 overhang parts.

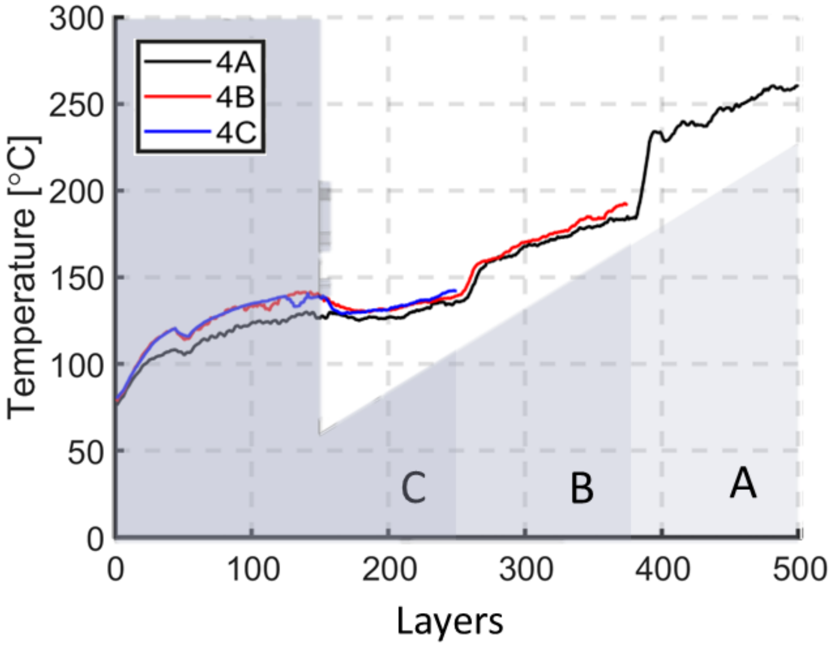

Figure 4-10: Extracted end-of-cycle temperature for sample heights built under nominal printing parameters (285 W, 960 mm/s). The infrared camera data shows that the B and C height samples have very similar end-of-cycle temperatures and can be considered thermal histories of each other, confirming the assumption that if sample A was stopped at the same height of B or C, they would have similar thermal trends. This overlap of end-of-cycle temperatures for A, B, and C heights is seen in all other parameter sets.

This IR data shows that while the parts have different heights, parts B and C (the shorter samples) have similar trends to Part A (Figure 4-10). This overlapping of the data is seen in the other six sets of parts. This concept of B and C being thermal histories of A is the cornerstone of the assumption made that if the samples labeled A were stopped at the same layer that parts B or C finished, they would have very similar meltpool depths and microstructures.

4.4.4 Graph Theory Review

The thermal modeling done in this research was done using an existing work and code base from Yavari *et al.* [41] , and Riensche *et al.* [39]. These works outline the use and functionality of Graph Theory to solve the heat equation and simulate temperature distributions in LPBF parts on a layer-by-layer basis. As developing a thermal model of the AM process is not the focus of this work, a relatively high-level overview of the process is given.

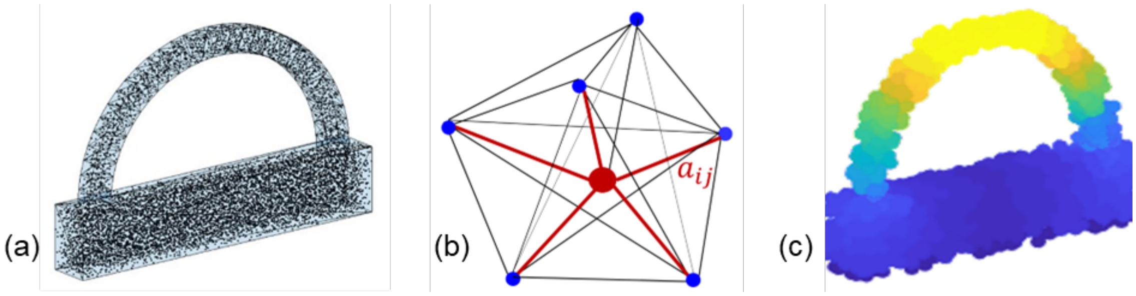

Figure 4-11: Depiction of how graph theory thermal simulation works. (a) nodes are generated in the CAD file, (b) nodes are connected, (c) thermal diffusion is performed (images courtesy of Alex Riensche).

To model the thermal history of a part using spectral graph theory, first a graph that corresponds to the real-world part needs to be created, Figure 4-11(a). This is done by randomly placing nodes into the part volume at a given density. From this, all the nodes can be connected to each other based on a set of rules and instructions, Figure 4-11(b). With a set graph, the heat diffusion equation is then solved with given process parameters, thermal conduction settings, and boundary conditions, Figure 4-11(c). The spectral graph theory approach replaces a continuous Laplacian with a discrete Laplacian matrix giving a first order differential equation. Solving this equation allows one to solve the heat diffusion loss at any time and location. A complete thermal history can then be obtained by repeating the Laplacian calculation and diffusion steps for all generated super layers of the part. A super layer is when, for simulation purposes, multiple real-world layers are combined into one layer [39], [41], [46]–[49]. A super layer size of 0.2 mm was used in this simulation. This resulted in a combination of five real layers per one super layer. Specifically, there are 100 simulated super layers for the 500 real layers of the A height parts, 75 simulated super layers for the 375 real layers of the B height parts, and 50 simulated super layers for the 250 real layers of the C height parts.

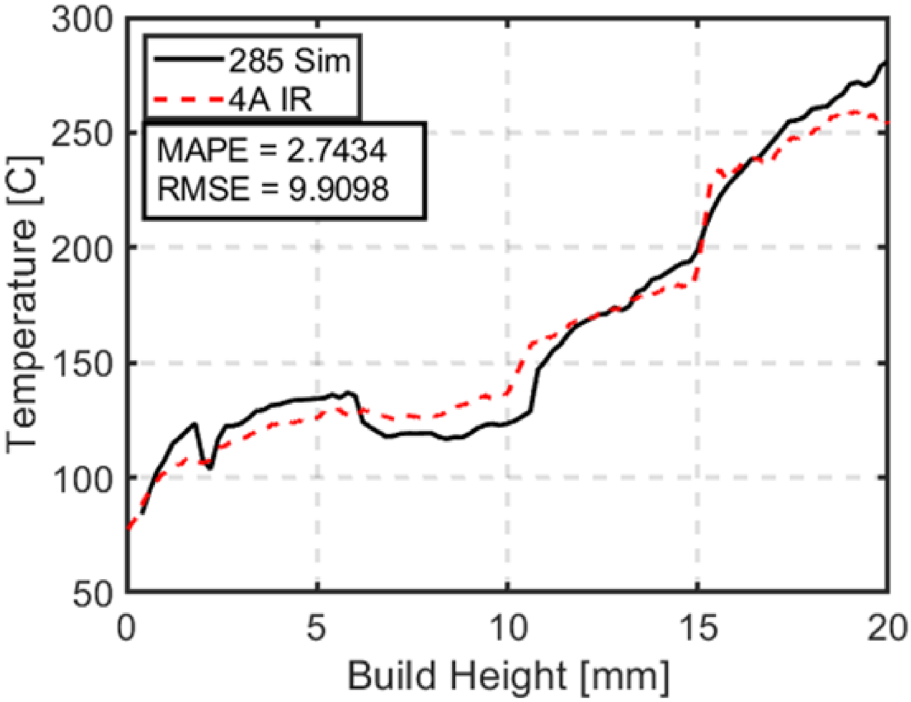

Figure 4-12: Comparison of graph theory thermal simulation (black) to real world infrared data (red). The accuracy is measured in terms of mean absolute percentage error (MAPE) and root-mean-square error (RMSE). The simulated end-of-cycle temperature was calibrated to the measured infrared end-of-cycle temperature by varying settings in the thermal simulation until the MAPE and the RMSE converged to the lowest found value of 2.74 % error and 9.91% error respectively.

The graph theory model was calibrated to the nominal machine parameter part at the tallest height, part 4A. This calibration was done by varying the setting for convection between the part and the powder and by varying the convection heat loss to the substrate at the bottom of the part. The value that was found was 2 $W \cdot m^{-2} \cdot K^{-1}$ for the heat loss to powder and 1600 $W \cdot m^{-2} \cdot K^{-1}$ heat loss to substrate.

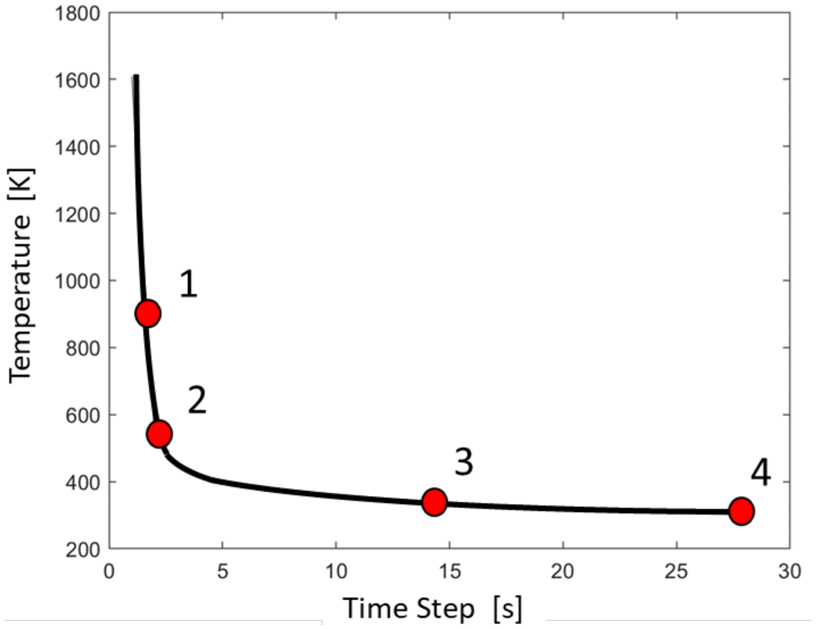

Figure 4-13: A single layer from the graph theory thermal simulation. Temperature values extracted, 1) Full width Half Maximum (FWHM), 2) Time step after FWHM, 3) Temperature at mid-point between FWHM and end-of-cycle temperature, and 4) End-of-cycle temperature.

From these calibrated thermal simulations, the last 3 super layers were evaluated as they were the closest to the measurement of meltpool depth. From each of these super layers, four values were extracted and visualized in Figure 4-13 and are listed below:

1) Full width Half Maximum (FWHM)
2) Time step after FWHM
3) Temperature at mid-point between FWHM and End-of-Cycle temperature
4) End-of-Cycle temperature

The FWHM value was chosen to capture the start of the rapid cooling that occurs after the laser strike. The data point one time step after the FWHM was chosen to not miss the steepness of the cooling curve. The mid-point between the FWHM and end-of-cycle temperature, and the end-of-cycle temperature were chosen as the last two values to denote the slowing or the cooling as it reaches closer to a steady state.

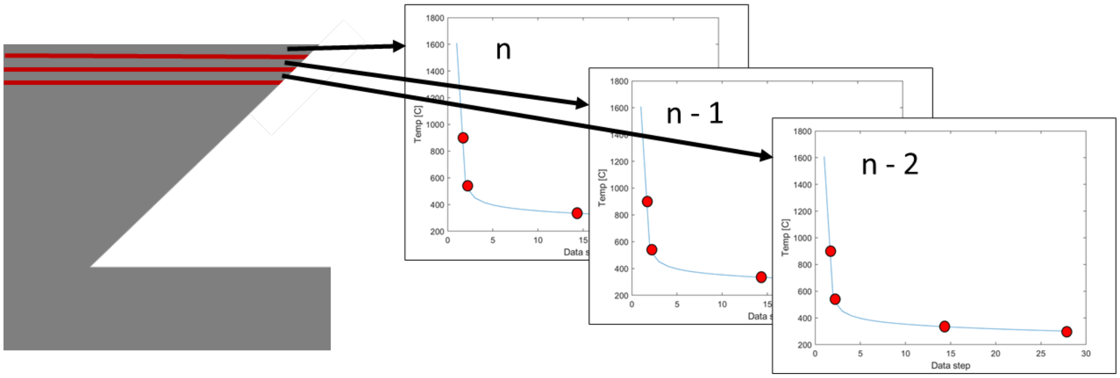

Figure 4-14: Visualization of the four simulation data points being extracted from the top three super layers creating 12 graph theory simulation data points to be used as features.

The four temperature values were extracted from the last three super layers at similar time steps, producing an additional 12 features (Figure 4-14). The simulations were repeated and recorded for each power and scan speed setting.

4.5 Review of Machine Learning Models

In this section, five models are discussed, with four being Machine Learning models and one being a statistical linear regression model. How each model operates will be explored and explained in this section. There is terminology that is consistent throughout many of these models and much of machine learning. There are two predictive modeling methods that are used which are classification prediction and regression prediction.

Classification can either be supervised or unsupervised learning in which the model categorizes a set of data into classes or target groups. If supervised learning is being performed, then the classes are labeled by hand, otherwise unsupervised learning allows the model to generate clusters based only on the data. In supervised classification models, the goal is to predict which target group a new set of data points belongs to. This is a powerful tool if the prediction resolution desired is low and can be binned into separate classes [20], [50].

Regression prediction is when an exact value is predicted in place of low resolution classes. Regression does not cluster the classes over a range like classification but uses all the raw output (measurement) values as targets. In short, regression modeling is predicting a continuous precise target for each input set of data [20], [51].

A *Feature* is an input into a model for both classification and regression; it is what is fed into the model to get a prediction [20], [50]. For each output there can be many input features that are used and are called a feature set. These feature sets can be generated by using the raw data, extracting statistical features from the data, or be physics-informed features extracted from the process being modeled. The best way to extract features for models is a major research thrust in practical machine learning papers [52]. In this work there are a total of twenty-seven physics and model-informed features that were extracted for potential use. Physics-informed feature extraction was chosen for this work because in previous work done by Smoqi *et al.* [53] and Liu *et al.* [54], it has been shown that the use of physics-informed machine learning enables the potential transferability of the created model to other geometries and machines in the AM process. Table 4-1 shows each feature and its source. How these features were extracted was described in greater detail in the previous sections.

Table 4-1: Feature set list organized by parameters, sensors, and graph theory model.

Parameters				
Power	Velocity	P/V ratio		
Sensor				
Area	Area STD	Major Axis	Minor Axis	Skewness
Eccentricity	ECT last 5 layers	Major Axis STD	Minor Axis STD	Skewness STD
Eccentricity STD	ECT STD			
Graph Theory Model				
(n) FWHM	(n) FWHM + 1	(n) Middle	(n) ECT	
(n-1) FWHM	(n-1) FWHM + 1	(n-1) Middle	(n-1) ECT	
(n-2) FWHM	(n-2) FWHM + 1	(n-2) Middle	(n-2) ECT	

The term *Ground Truth* is used to denote the real value that corresponds to the feature. So, in this data set of 27 features, there is one answer value that relates to each data point. An example of this can be seen in Figure 4-15.

$$\begin{array}{ccc} \underline{\text{Sample}} & \underline{\text{Feature Matrix}} & \underline{\text{Class}} \\ \begin{Bmatrix} 1 \\ 2 \\ \dots \\ m \end{Bmatrix} & \begin{Bmatrix} P/V_1 & sk_1 & . & T_1 \\ P/V_2 & sk_2 & . & T_2 \\ P/V_{\dots} & sk_{\dots} & . & T_{\dots} \\ P/V_m & sk_m & . & T_m \end{Bmatrix} & \begin{Bmatrix} C_1 \\ C_2 \\ C_{\dots} \\ C_m \end{Bmatrix} \end{array}$$

Figure 4-15: Depiction of how each sample has a corresponding row in the Feature Matrix and Class target. In the Feature Matrix, each column corresponds to a feature that has be extracted or created and a Class. The Class array contains the ground truth that was measured.

Figure 4-15 shows a representative excerpt of the total data set used. Each column in the feature matrix is related to a specific feature such as skewness, and each row is related to a specific data point with an output of class on the right. These features and outputs are split into the three classification regimes of meltpool depth performed in this work, described in section 4.2. The split performed is an even split of the data to ensure that each class of data has an equal number of data points for training and testing. This type of split is to ensure that there is no bias introduced into the model based on uneven data distribution. If this was not done there could be bias in the prediction, where the model would more often predict one class or value more often because it is getting this as a ground truth disproportionally more than other answers.

With properly selected data, the first step in implementation of the models is the optimization of the hyperparameters. For this work, MATLAB's default Bayesian hyperparameter tuning toolbox was used for each model applied. Each model has a different set of hyperparameters that needs to be tuned and are discussed in more detail in their respective sections. These parameters were then used in the training of the subsequent models. In all the models used, an 80-20 train-test split was performed. This means that 80% of the curated data is used for training, and the remaining 20% of the data is used for testing. Training is when the model is given both the feature set and the target (label) so that it can 'learn' the models' respective constraints and weights. Testing is when the model is given only the feature set of data and attempts to predict the output target. This predicted target is then compared to the actual target label for the determination of model fidelity. This type of train-test split helps to ensure that the model is not overfitting to a certain subset of data. To further determine the robustness of the model, the data was randomized 10 separate times, and after each randomization an 80-20 train-test iteration occurred. The result of each iteration was used to determine the model fidelity and robustness. The performance metrics used to determine the fidelity of each type of model are the F-Score (classification) and R^2 (regression).

4.5.1 Classification: F-Score

The F-Score is the performance measure that evaluates a binary system's performance, such as a two-way classification. This metric uses the predicted model's precision and recall to inform its fidelity. For this data set, F_1-Score was used interchangeably with F-Score. F-Score and confusion matrices are commonly used together to fully describe the performance of a classification system.

A confusion matrix, shown in Figure 4-16, is a table that visualizes the results of a model. In the columns, it shows the predicted class from the model, and the rows demarcate the actual class, which is the ground truth. The diagonal holds the true positive and true negative values. The true positive is the number of positives correctly identified by the model, and the true negative is the correctly identified negatives by the model. A model with an F_1-Score of 1, which is the highest value and is 100% accuracy, would have all of its tested values in these locations. The other locations are where the model incorrectly identified the classes. These are the false positive (type 1 error) and the false negative (type 2 error); this is where the model is not correctly identifying the values. The F-Score uses these values, true positive, true negative, false positive, and false negative to account for both type-1 and type-2 errors in its fidelity measurement [52].

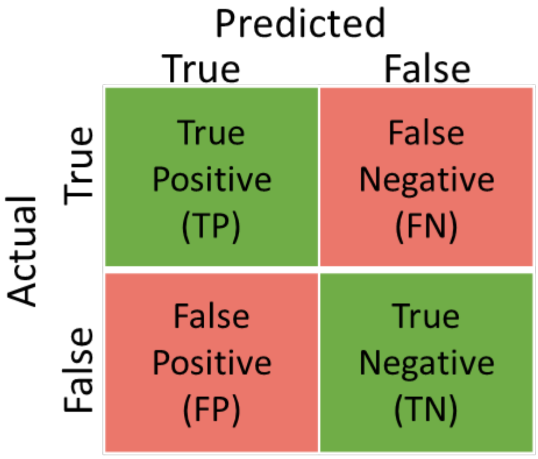

		Predicted	
		True	False
Actual	True	True Positive (TP)	False Negative (FN)
	False	False Positive (FP)	True Negative (TN)

Figure 4-16: Example of confusion matrix that contains the number of True Positives (TP) and True Negatives (TN) along the diagonal. These are the amount of times the model correctly predicted the class of the inputted features. A model with 100% accuracy would have all values within these locations. The False Negative (FN) and the False Positive (FP) are when the model incorrectly assigns a class. This matrix will always be a square matrix n-by-n, where n is the number of classes used.

F_1-Score is the harmonic mean of recall and precision that weights the precision and recall evenly. There is a generalized F_β-Score that allows for the precision or recall to be weighted more heavily depending on its importance and use case. The equation for the F_1-Score (the standard F-score used in machine learning) is:

$$F_1 = 2 \times \frac{1}{{}^{1}/_{\mathrm{recall}} \times {}^{1}/_{\mathrm{precision}}} = 2 \times \frac{\mathrm{precision} \times \mathrm{recall}}{\mathrm{precision} + \mathrm{recall}} \tag{2}$$

Precision is the measure of the true positives (TP) and false positives (FP). It is a fraction of the true positives divided by the false positives plus the true positives:

$$\mathrm{Precision} = \frac{\mathrm{TP}}{(\mathrm{FP} + \mathrm{TP})} \tag{3}$$

Recall is measure of the true positives (TP) and false positives (FN). It is a fraction of the true positives divided by the false negatives plus the true positives:

$$\text{Recall} = \frac{\text{TP}}{(\text{FN} + \text{TP})} \tag{4}$$

The F_1-Score equation can be rewritten as:

$$\text{F}_1\, Score = \frac{TP}{TP + 0.5(FP + FN)} \tag{5}$$

4.5.2 Regression: R^2

The coefficient of determination, or R^2, is a measure of the goodness of fit of a model to the actual data, or ground truth. While F-Score relates accurately from a Classification model, R^2 relates the accuracy of a Regression model.

$$R^2 = 1 - \frac{Unexplained\ \times Variation}{Total\,Variation} = 1 - \frac{\sum(y_i - \hat{y}_i)^2}{\sum(y_i - \bar{y}_i)^2} \tag{6}$$

This total sum of residuals squared is the unexplained variation of the model. In the denominator there is the sum of squares, which is the difference a data point is away from the mean squared; this summed gives the total variation. R^2 will have values ranging from 0 to 1, where 1 is a perfectly fit model to the data [55]. A Regression Relation can be seen in Figure 4-17. This figure shows the actual values on the x axis and the predicted values on the y axis. If this model were to have 100% accuracy all values would line up on the x-y diagonal in blue.

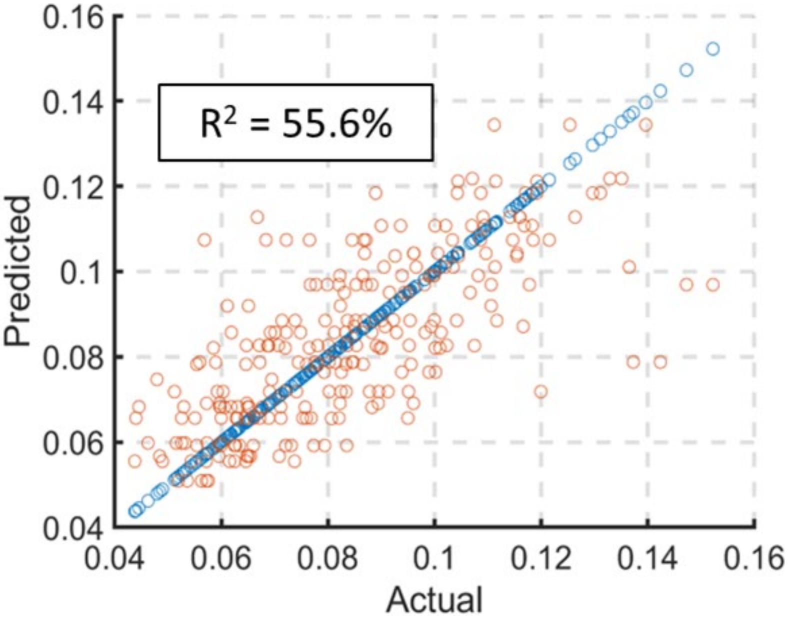

Figure 4-17: Visualization of the R^2 value's relationship to actual regression predictions. The actual ground truth measured value is on the x-axis and the model predicted value is on the y-axis. This visualization is used to express how accurate a model is; the more accurate the prediction the closer the values would be to the diagonal.

4.5.3 Conventional Statistical Models

Conventional statistical regression models were the simplest of the models used, as they do not have any active learning. Multinomial logistic regression was used for classification prediction and linear regression was used for regression prediction. Multinomial logistic regression is used to do categorical placement of data. It is based on binary logistic regression and is done by taking a maximum likelihood estimation that then evaluates the probability of categorical placement or which class the inputs belong to [52].

Linear regression looks to predict a dependent variable value (meltpool depth) from given independent variables (features). This is done by finding linear relationships between the input (feature set) and output (meltpool depth). The underperformance of these models shows the need for more intensive models such as machine learning models.

4.5.4 K-Nearest Neighbor Networks (KNN)

The K-Nearest Neighbor Network (KNN) is a simple supervised model that operates on the idea that similar outcomes are in proximity to each other (Figure 4-18). This clustering was done using a Euclidean distance calculation of the L_2 norm; there are other distance equations that can be used to create the groups or neighborhoods, such as Manhattan distance, however Euclidean distance is the standard used in this work. The Euclidean distance calculation can be seen below:

$$Dist(a, b) = \sqrt{(a_x - b_x)^2 + (a_y - b_y)^2} \tag{7}$$

This equation takes in the features and their associated target and evaluates the nearness to known groups from the training of the model. The K in KNN determines the number of nearest neighbors to compare when determining which group the new data point belongs too. This value should always be an odd number so that there are no ties between classes in the model. K-Nearest Neighbor Networks are susceptible to bias created by the number of data points in a class, wherein if a class has disproportionately higher representation it will skew the results to that class [50]. This was overcome by creating an even split of classes as previously discussed in section 4.2.

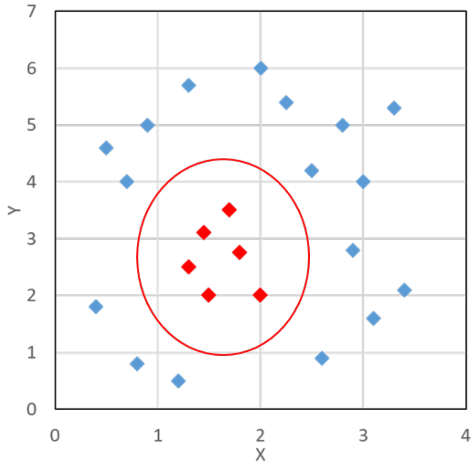

Figure 4-18: Visual representation of how a K-Nearest Neighbor Network operates. K-Nearest Neighbor Network finds groups of similar answers and compares new data points to the nearest known group from the training data set. This is done by finding the distance from the training data points to the new data point and taking the "k" nearest neighbors. These neighbors then vote based on their class which class the new data point belongs to. These votes are summed and the class with the most votes is then assigned to the new data point (image courtesy of Dr. Sam Gerdes).

An example of a KNN clustering can be shown in Figure 4-18, where the new data point is added. This data point's distance to all the other points was found first. Then the model takes the closest K neighbors and assigns it a class based on the "vote" or class each neighbor belongs to [50].

It is important to note that KNN can be used as an unsupervised machine learning model to generate clusters based solely on the data set and the number of desired clusters. However, this application of the KNN was not used in this work as the classes were determined manually via metallurgical analysis.

4.5.5 Support Vector Machines (SVM)

Support Vector Machines (SVM) are a supervised learning method that can be used for classification and regression prediction. A SVM's goal is to create a hyperplane in a higher dimension rather than that of the feature set dimension. This is accomplished with the kernel function, where the model is able to project the data into a higher dimension. The kernel function used in this work is the radial basis function. Hyperplanes are the decision boundaries of the model, where depending on which side the data point falls determines its class or value. These hyperplanes that the model creates are attempting to generate the maximum-margin between the difference in the classes data. This maximum-margin is determined via the support vectors generated along the boundary points of given classes. Support vectors are vectors formed using only the data points found to be on the edge of a given class of data. The support vectors of two adjacent clusters are then compared to each other to find the maximum-margin between the two vectors in which to place the hyperplane on [50], [56].

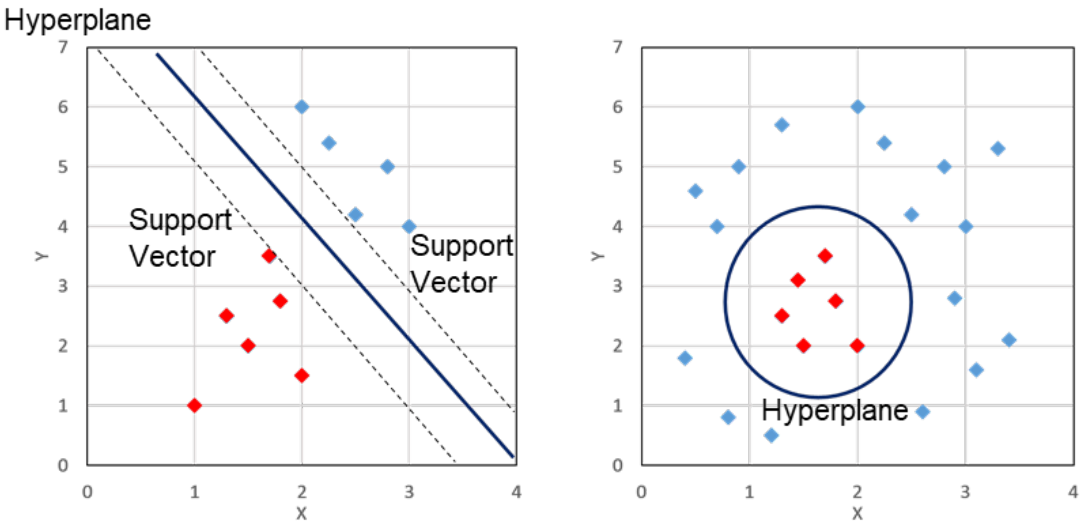

Figure 4-19: Support Vector Machines training data was inputted and becomes the higher dimension map. This higher dimensional map is determined by a kernel function and then support vectors place the hyperplanes that separates the groupings (image courtesy of Dr. Sam Gerdes).

4.5.6 Random Forest Networks (RF)

A Random Forest Network (RF) is a supervised machine learning algorithm that uses a collection of random decision trees. Each node in the forest is a decision based on the inputted training features that then branches off into another node. This sends the data down the network through each decision node until the last node, which has the class or regression value; this last node is denoted as a leaf. The training data is used to form many different decision trees; these trees make up the forest. After training, the testing data or new datapoints are run down each tree where the final predictions are done by majority rule at the last leaf in every tree [56]. Figure 4-20 shows an example of this process. This model is called a random forest because it generates a random number of trees, branches, and leaves within a user defined boundary. In this way, each decision the model makes is un-biased due to the randomized nature of its creation. A distinct advantage of basic decision trees is that they have a high level of bias.

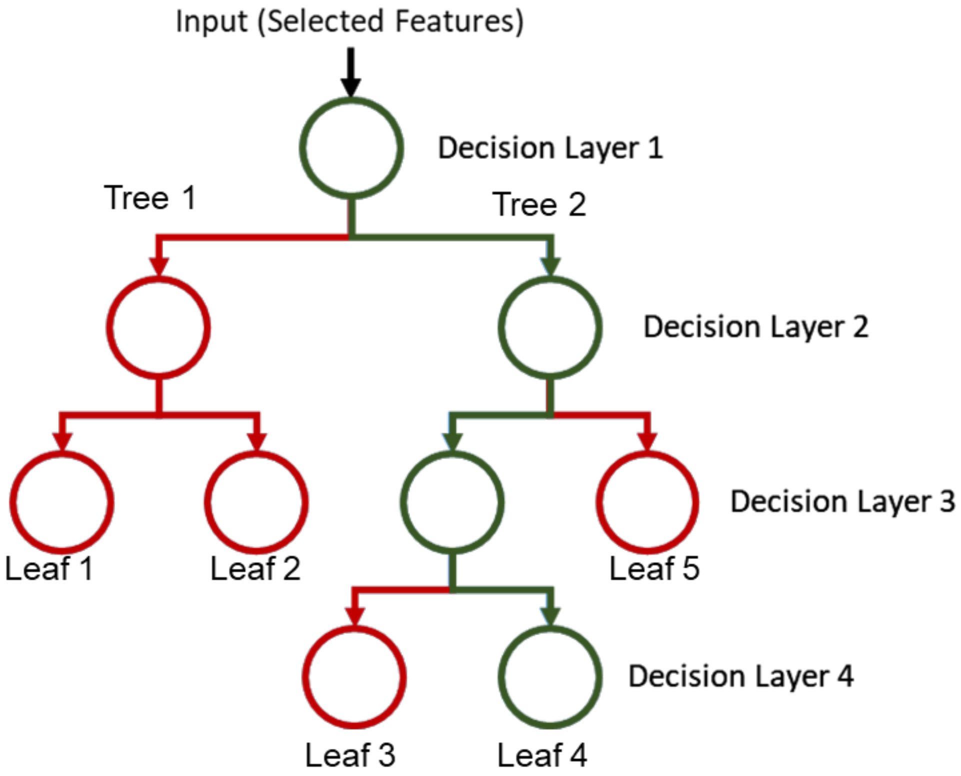

Figure 4-20: Random Forest Network with an input of a new data point. The first decision tree sends that data set down a branch and down each tree until the final leaf. The final predictions are done by majority rule at the last leaf in every tree (image courtesy of Dr. Sam Gerdes).

4.5.7 Artificial Neural Networks (ANN)

The Artificial Neural Network (ANN) that was used in this research was a multilayer perceptron (MLP). A MLP is a fully connected feed-forward ANN and is generally regarded as the simplest ANN model. This network uses a minimum of three layers, an input layer, a hidden layer, and an output layer. Additional hidden layers can be added to change the structure from a shallow neural network (1-3 hidden layers) to a deep learning neural network (>3 hidden layers). The basic structure of the ANN is an input layer which holds the feature set for a given point to be evaluated; this then sends the inputs into the first hidden layer by multiplying each input layer node by an associated weight (W_{ij}), which houses the neurons. In the neuron, the summation of the weighted input layer neurons is fed into an activation function (usually based on the softmax function) to normalize the value. The neuron's output from the first hidden layer is then sent into subsequential layers, using the same process of multiplying weights and normalizing with activation functions, until the final hidden layer. At which point, the values are fed into the output layer that performs either the classification or regression prediction [57].

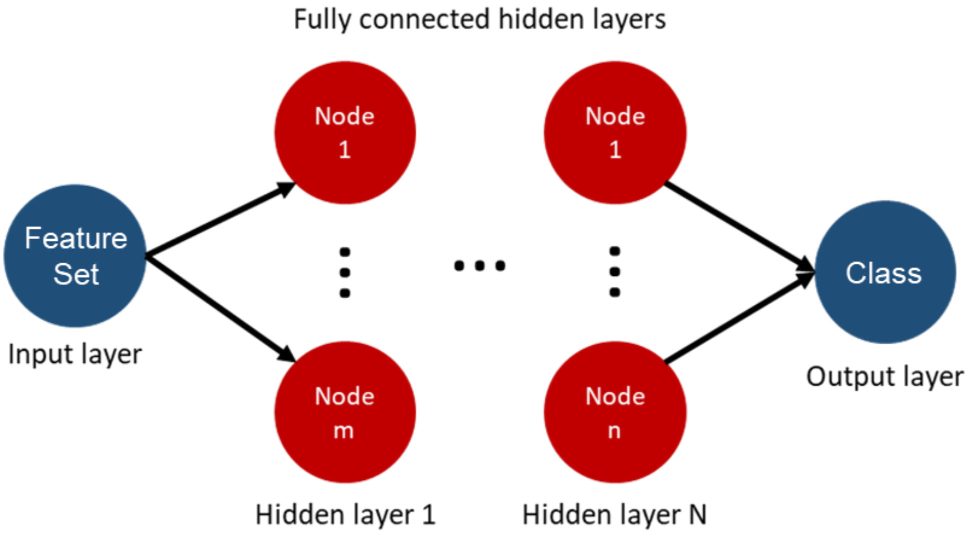

Figure 4-21: Schematic for Artificial Neural Network, this network has three main sections, an input layer, hidden layers, and an output layer. The input layer is made up of the feature set. This incoming data is then weighted and fed into a neuron. The neuron sums the weighted inputs and outputs this sum to an activation function. This function then determines the output of the neuron and feeds this into the next layer. After "N" layers the results are place into the output layer (image courtesy of Dr. Sam Gerdes).

Each node or neuron is connected and has weights for every input from the previous layer. At the neuron, the weighted inputs are summed, and that value is passed into the activation function. The activation function takes in this sum and based on the applied function, decides the neuron output. Activation functions can take many forms, the most basic is a step function, where if the input is greater than a set threshold, the neuron activates. A common activation function is the hyperbolic tangent sigmoid transfer function which was used in this work. The MLP model learns its weights via the back propagation method. This method finds the error in the predicted output in comparison to the actual value. It then back propagates the error through the model to modify the weights connecting every node to account for this error in prediction. It then repeats this for every feature set in the training data [57].

CHAPTER 5 – RESULTS

This chapter reports the results of extracted features as inputs into various machine learning models for the prediction of meltpool depth. In section 5.1 contains the results for the meltpool depth characterization. Section 5.2 includes an overview of the meltpool shape characterization, particularly the meltpool area. This section additionally includes the correlation that was found between the meltpool pool area and depth and the discussion of the extracted data from the infrared camera. In section 5.3 all the features that were discussed in previous sections are presented and methods for feature selection are described. Section 5.4 contains the results of the prediction of meltpool depth. Lastly, in section 5.5 there are the results for the visual representation of the primary dendritic arm spacing when compared to thermal data.

5.1 Meltpool Depth Characterization

Using the technique that was laid out in section 4.1, all twenty-one parts' top surface meltpool depths were measured. The results of these measurements are seen in Figure 5-1 to Figure 5-3.

Figure 5-1 shows the nonlinear relationship between the power-velocity ratio and the meltpool depth. As the energy density or P/V ratio increased one would expect an increase in meltpool depth, similar to the end-of-cycle temperature trend discussed, but this was not seen in this data. At the lower energy density/lower power regions (red) there was a relatively low meltpool depth.

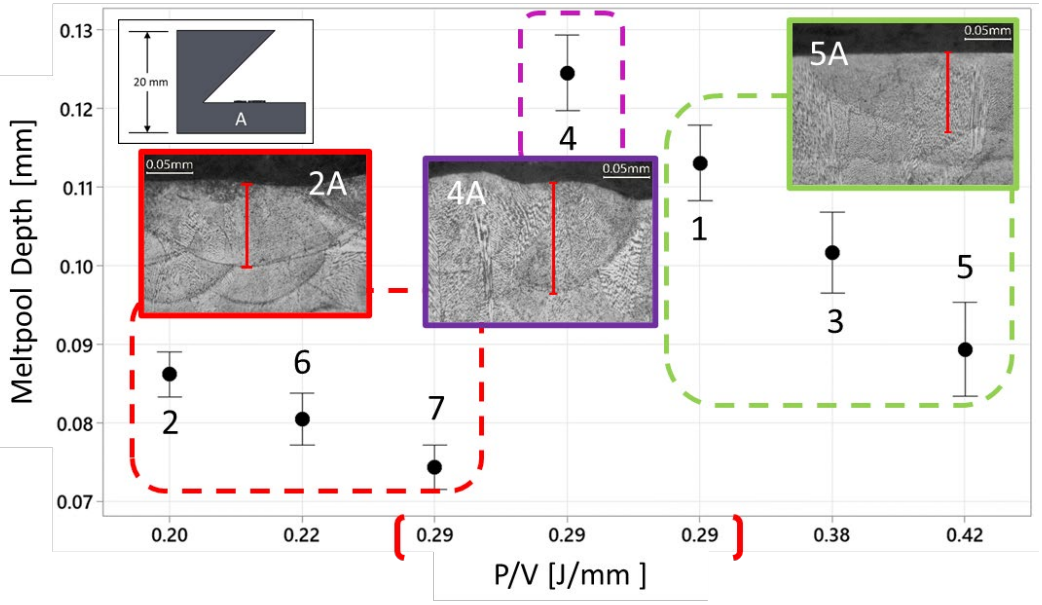

Figure 5-1: Mean meltpool depth [mm] for the last layer for A heights versus the power-velocity ratio (P/V [J/mm]). Lower P/V ratios resulted in smaller meltpool depths. Samples 2 and 6 have less penetration (red). Samples 7, 4, and 1 have similar P/V ratios. Sample 7 has the lowest power and scan speed and has relatively small meltpool depth. When the power and scan speed were increased to the nominal (purple) settings, there was a large increase in meltpool depth to approximately three layers penetration, which was expected for the nominal setting. As the P/V ratio was increased, an increase in meltpool depth was expected but as seen in samples 1, 3, and 5 (green) there was a decrease in meltpool depth at the higher P/V ratios.

When the samples with similar P/V ratios were explored, it was seen that there was no strong correlation between the P/V ratio and meltpool depth. The nominal setting sample (purple) shows a higher meltpool depth which was an optimal meltpool depth for this part. At the higher energy density regions (green) there were relatively moderate meltpool depths. In this region there was less penetration than expected. Each A height sample was measure approximately 70 times per part.

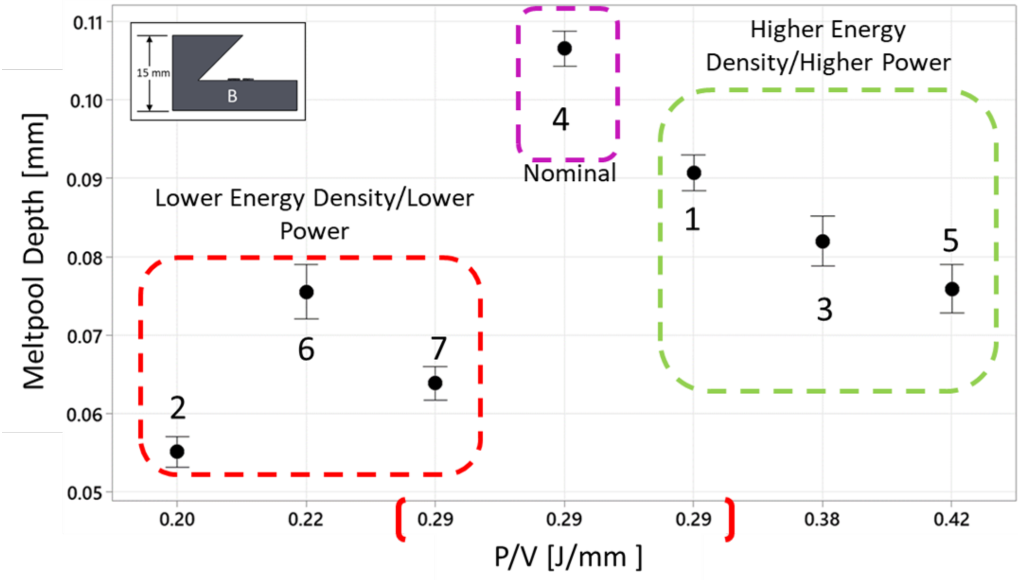

Figure 5-2: Mean meltpool depth [mm] for the last layer for B heights versus the power-velocity ratio (P/V [J/mm]). Similarly to the A heights meltpool depth measurements, the region of lower energy density/lower power (red) had relatively lower meltpool depth. The nominal (purple) had the highest meltpool depth and the region of higher energy density/higher power (green) had meltpool depths in between the low and the high measurements.

Figure 5-2 shows similar nonlinear trends as Figure 5-1, where the meltpool depths are low at the lower energy density region and then there was a jump at the nominal setting. Again, the nominal setting parts have an optimal meltpool depth. As the P/V ratio increased, the meltpool depths began to fall off and decrease. Each B height sample had approximately 100 meltpool depth measurements per part.

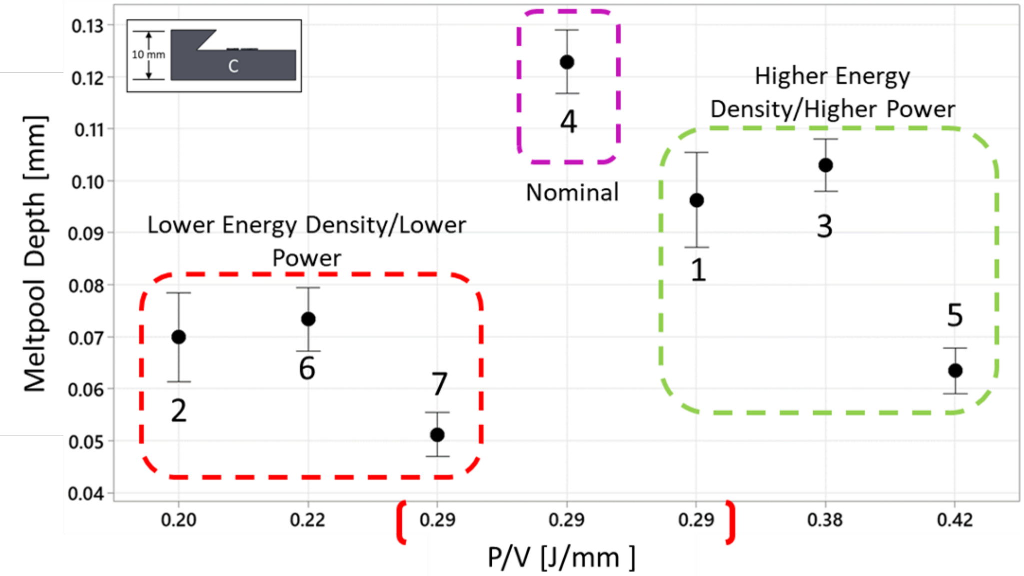

Figure 5-3: Mean meltpool depth [mm] for the last layer for C heights versus the power-velocity ratio (P/V [J/mm]). There was a similar trend in C heights as seen in the A and B heights. The region of lower energy density/lower power (red) have relatively lower meltpool depths, while optimal depths are seen at the nominal settings (purple). Lastly, the region of higher energy density/higher power (green) has meltpool depth measurements that decrease when compared to the nominal setting parts.

Each C height sample had approximately 20 meltpool depth measurements per part. Figure 5-3 shows the same nonlinear trend that was seen in the A and B heights. This nonlinear trend helped inform the decision to use machine learning. Machine learning models can find correlations in feature sets that are non-linear. The anticipated trend was for there to be a constant increase in meltpool depth, as the energy density increased, but this was not seen. The energy density was not a good predictor of meltpool depth; there was a relationship that was not apparent. The excess energy applied at higher energy densities did not increase meltpool depth (Z direction), however, that energy must go somewhere. Since the meltpool depth did not increase, the next logical place for the energy to dissipate through is in the X-Y plane, increasing the meltpool area. This will be investigated in the next section via the discussion of meltpool area that was extracted from the imaging pyrometer.

5.2 Correlation of Sensor Data and Meltpool Depth

Using the techniques that were laid out in section 4.4 all twenty-one parts' top surface meltpool shape features were extracted from the imaging pyrometer. This allowed for the data's relationship to the meltpool depth to be explored. The methodology for extraction of end-of-cycle temperature from the IR sensor data was previously discussed in section 4.4.3. Using this technique, the end-of-cycle temperature was extracted for the last five layers of each part.

5.2.1 Meltpool Pyrometer Characterization

With the pyrometer data processed the shape features were extracted. This allowed for a qualitative analysis of the meltpool images. As meltpool shape features are highly correlated, only the meltpool area will be explored in these characterization results. The other meltpool shape features have similar trends to the meltpool area, therefore meltpool area was chosen to be presented as an overall portrayal of these features. Representative images were found for each of the parameter settings for the A heights. This was done by finding the mean number of pixels in the meltpool area, major axis, and minor axis for each parameter. The values were used to select a frame from the part data that had approximately the same size and shape.

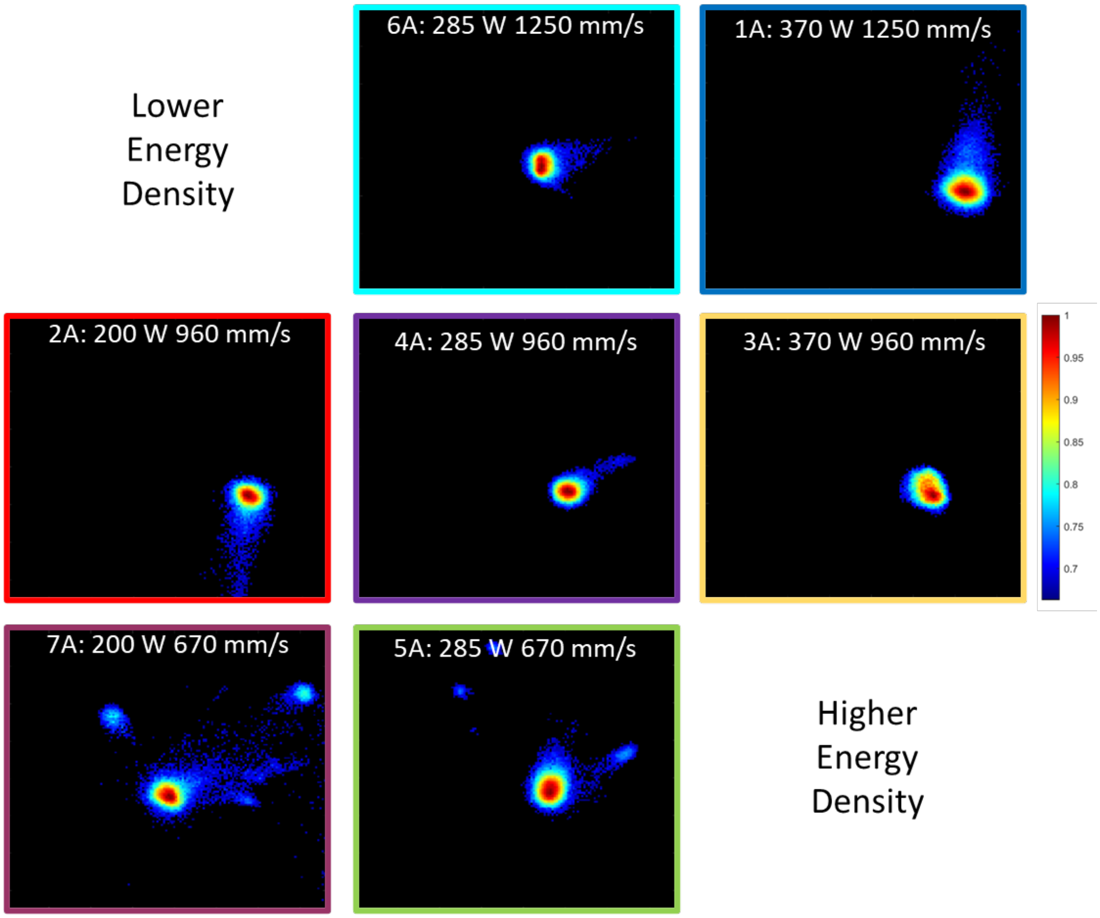

Figure 5-4: Images representing the mean meltpool shape of each part. The meltpool area increased as the power setting increased. This was seen in the center three parts' data (2A, 4A, 3A) and across the diagonal (7A, 4A, 1A) whereas the power was increased and the overall shape of the meltpool widened giving a larger area. The lower power parts (2A, 7A) had a relatively small area. The nominal setting (4A) had a relatively small meltpool. The higher power parts (1A, 3A) had a relatively higher meltpool area. The parts along the vertical (6A, 4A, 5A) showed a trend where the velocity decreased and the area increased. This image had the same layout as the power and velocity schematic (Figure 3-6).

In Figure 5-4 meltpool images representing the mean meltpool shape of each part are shown. These meltpool images have the same layout of power and velocity setting that was seen in Figure 3-6, where the power and velocity was changed by ± 30% from nominal. These meltpool images show a general trend of meltpool area increasing as power settings were increased when compared to the nominal parameter meltpool. The samples that had similar energy densities show an increasing meltpool area as the power was increased. Lastly, as the velocity decreased, the meltpool area increased.

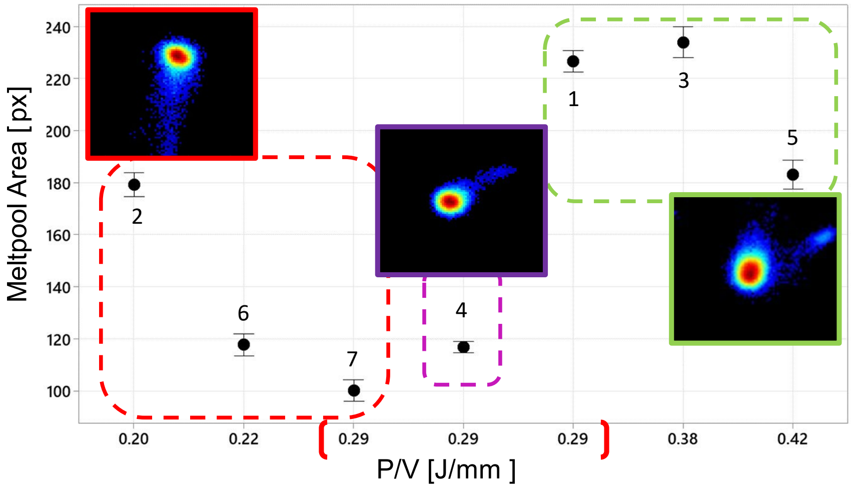

Figure 5-5: Mean meltpool area [px] for the last layer for A heights (P/V [J/mm]). The general trend that was seen in the meltpool area was that meltpool area increased at the higher power settings. Parts 6 and 7 show small meltpool areas (red). The nominal part 4 (purple) also shows a small meltpool area. As the power was increased, relatively large meltpool areas were seen in parts 1, 3, and 5 (green). Part 2 had a relatively medium area meltpool which was unexpected. When further explored, it was believed to be from meltpool instability, where part 2 had the largest skewness in the meltpool intensity.

Figure 5-5 shows the mean meltpool area for the A heights. In this figure a general trend was seen, the meltpool area increased as the power settings increased. This was seen in parts that had similar energy densities. Part 7 had the lowest power and a smaller meltpool area. The power was then increased to the nominal settings for part 4, and a small increase in meltpool area was seen. The power was further increased for part 1 and a large jump in meltpool area was observed. Parts 3 and 5 had a higher energy density and higher meltpool areas when compared to the nominal settings part. Part 2 had a relatively medium meltpool area, which was unexpected. When further explored this was believed to be from meltpool instability, part 2 had the largest skewness in the meltpool intensity. This increased skewness meant that the distribution of heat in the meltpool had more outliers of higher intensity pixels. These higher intensity pixels would be a result of a hotter meltpool. This reflects the results seen in the meltpool area figures in this section and in the end-of-cycle temperature figures in section 5.2.2.

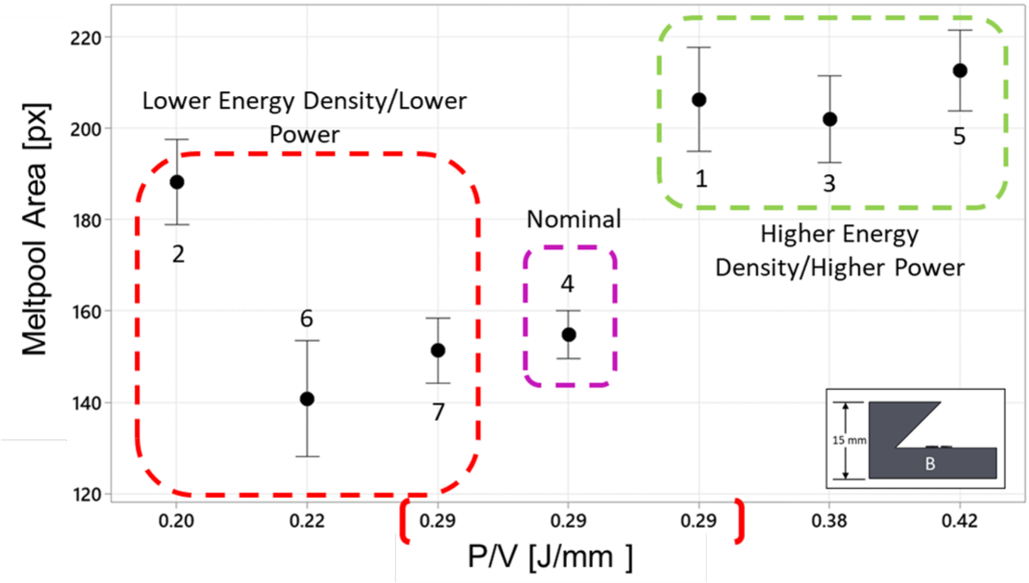

Figure 5-6: Mean meltpool area [px] for the last layer for B heights versus the power-velocity ratio (P/V [J/mm]). Similar trends to the A heights meltpool area measurements where, sans part 2, the lower power region (red) had smaller meltpool areas and the nominal part 4 (purple) also showed a relatively small meltpool area. Like A heights, there was the same jump in meltpool area as the power increased to the higher power region (green).

The B heights had a similar trend to the A heights, when the power increased in the region of similar P/V ratios, there was an increase in the meltpool area. The mean meltpool areas for B heights can be seen in Figure 5-6. In addition to this trend, the general locations of the data in the A heights were mirrored in the B height data. The region of lower energy density/lower power had the smaller to medium meltpool areas and the higher energy density/higher power region contained the largest meltpool areas.

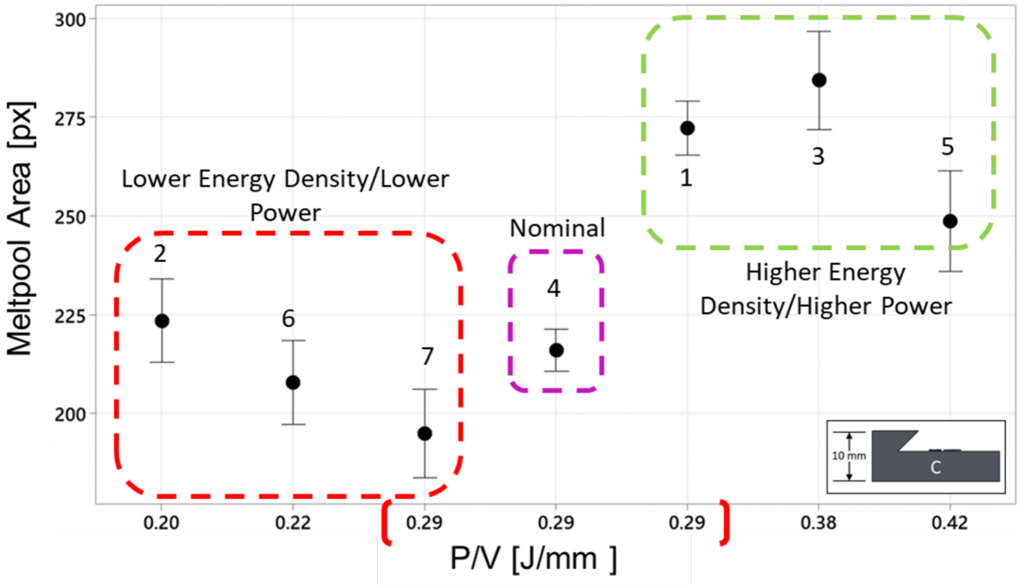

Figure 5-7: Mean meltpool area [px] for the last layer for C heights versus the power-velocity ratio (P/V [J/mm]). The area trends extracted for the C heights were likewise to the trends seen in the A and B heights. The region of lower energy density/lower power (red) had relatively medium to small meltpool areas, along with the nominal (purple) having a relatively small meltpool area when compared to other C height parts. The higher energy density/higher power region (green) contained the larger meltpool areas. Lastly, a similar trend to the A and B heights, when the power increased in the region of similar P/V ratios there was an increase in the meltpool area.

Figure 5-7 shows the mean of extracted meltpool areas for the C heights. This plot shows the comparable trends to the A and B height parts' meltpool areas. For parts of similar energy densities, as the power was increased, the meltpool area also increased. The lower energy densities had an overall small to medium meltpool area when compared to the nominal parameter settings and the higher energy densities had overall larger meltpool areas.

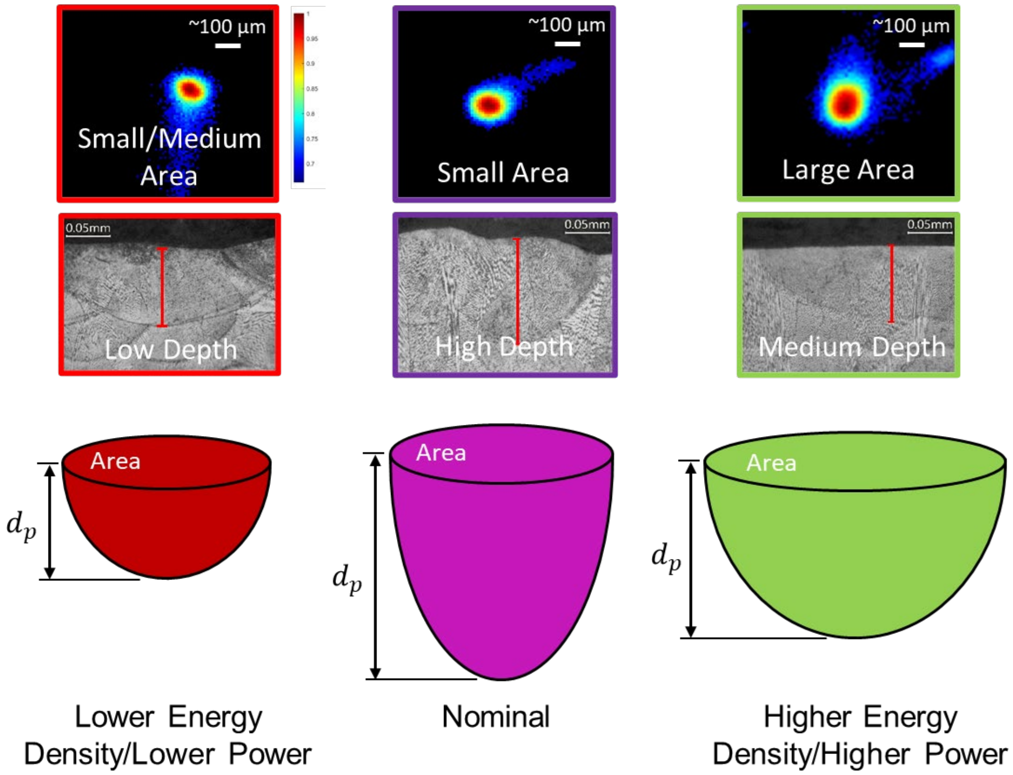

Figure 5-8: Meltpool depth and area correlations to power-velocity ratio. The lower energy density/lower power parts (red) had small to medium sized meltpool with relatively low meltpool depth penetration. The nominal parts (purple) had a small meltpool area with a high meltpool depth. The higher energy density/higher power parts (green) had a larger meltpool area with a medium depth. A nonlinear relationship was observed between the depth and area of the meltpool. Meltpool area increased at higher energy density. It is hypothesized that there was a breakdown in penetration of the meltpool and instead of a continuously increasing meltpool depth there was a point where the energy started to widen the meltpool. Once there was too much power or energy in the meltpool, it began to spill over into the surrounding horizontal directions, giving a larger meltpool area, as seen in the higher energy density region.

Figure 5-8 shows the correlation between the meltpool pool area, depth, and energy density. A nonlinear relationship between depth and area of the meltpool was observed in these measurements. Compared to the nominal setting, the higher energy densities had larger meltpool areas but there was a loss in meltpool depth. This is due to the heat dissipating towards the melting of the surrounding powder instead of downwards toward the previous layers. Simply stated, the higher energy densities resulted in the excess melting of powder and a reduction in meltpool penetration from nominal.

5.2.2 Infrared Camera Characterization

The end-of-cycle temperature was extracted for the last five layers of each part and the mean and standard deviation was found. From the IR camera and the extracted end-of-cycle temperatures, it was determined that energy density was an insufficient predictor of end-of-cycle temperature. This can be seen in Figure 5-9 where the three parts which had similar P/V ratios did not share similar temperatures. As the laser power increased and the P/V ratio stayed the same, there was an increase in end-of-cycle temperatures.

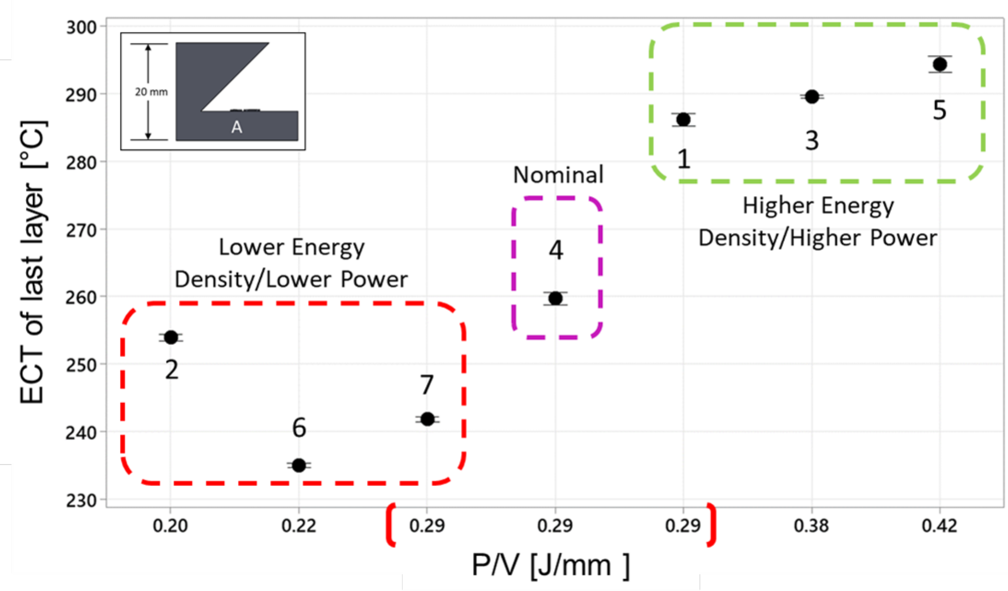

Figure 5-9: Mean end-of-cycle temperature [°C] for the last five layers correlation to power-velocity ratio (P/V [J/mm]) for A heights. The three settings that have similar P/V ratios (7, 4, 1) do not have similar temperatures; this shows that energy density was not a good predictor of end-of-cycle temperature. These three settings also show that as the power increased there was an increase in end-of-cycle temperature.

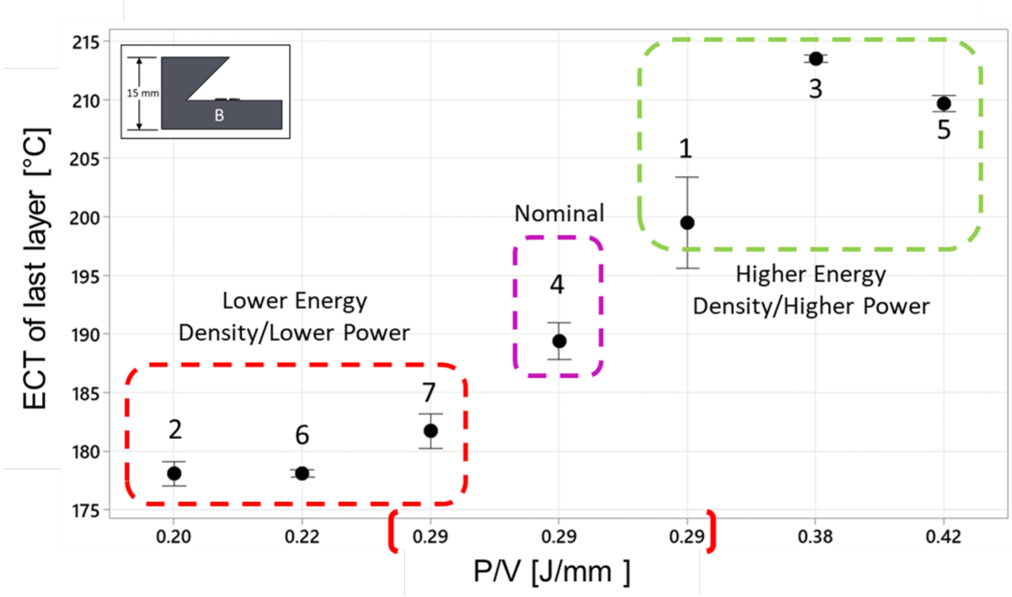

Figure 5-10: Mean end-of-cycle temperature [°C] for the last five layers versus to power-velocity ratio (P/V [J/mm]) for B heights. These values have a similar trend to the A heights, where the lower energy density/lower power parts (red) have a generally lower end-of-cycle temperature and the higher energy density/higher power parts (green) have a higher end-of-cycle temperature.

Similar trends are seen in Figure 5-10 and Figure 5-11, where similar P/V ratios show there was not strong correlation between energy density and end-of-cycle temperature but there was a correlation between the power and end-of-cycle temperature. There was also clustering with the lower power parts experiencing lower end-of-cycle temperature and the higher power parts a higher end-of-cycle temperature.

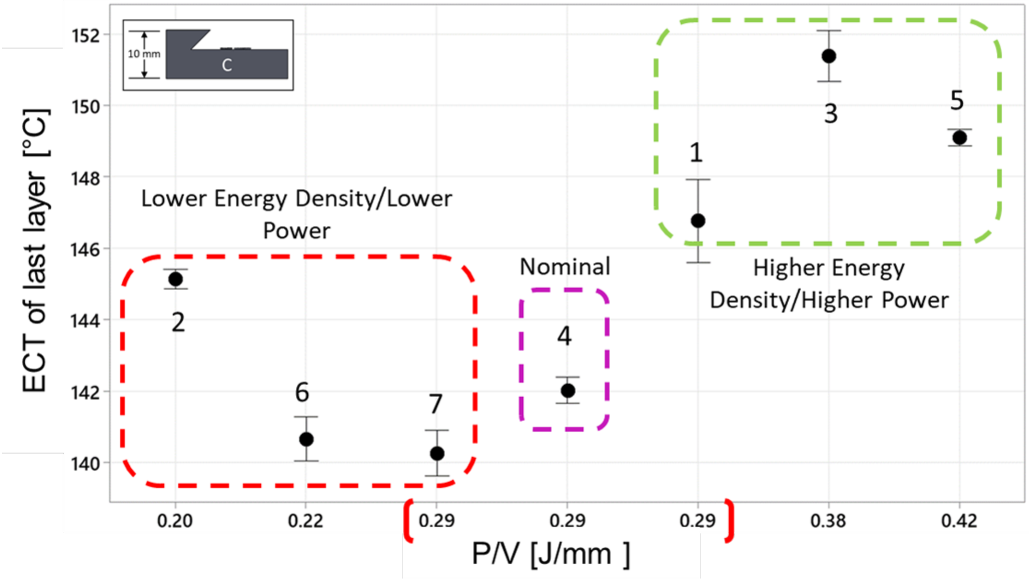

Figure 5-11: Mean end-of-cycle temperature [°C] for the last five layers compared to power-velocity ratio (P/V [J/mm]) for C heights. Like trends in C height parts, as seen in A and B height parts. The same trend was seen when three settings, that had similar P/V ratios (7, 4, 1), do not have similar temperatures which showed as the power increased, end-of-cycle temperatures also increased. This demonstrated that energy density was not a good predictor of end-of-cycle temperature.

The trend seen in the end-of-cycle temperature for all three part heights clearly shows that increasing laser power results in increased end-of-cycle temperature, implying the presence of heat accumulation. This data also showed that energy density should not be used as a predictor of end-of-cycle temperature.

5.3 All Features and Feature Selection

For evaluation of predicting meltpool depth through the use of machine learning models, three main categories were chosen, they are:

- Parameters (P)
- Parameters + Sensor (P + S)
- Parameters + Sensor + Graph Theory (P + S + GT)

For each of these categories, feature selection was done, and the five prediction models discussed previously were run. For the first category, Parameters, there was no feature selection done as there are only three features in this category.

For feature selection of the Parameters + Sensor category an evaluation of its features' Learning Curve was performed; these features used can be seen in Table 5-1.

Table 5-1: Features selected to be used in the prediction of meltpool depth classes.

<table>
<tr><td colspan="5">Parameters</td></tr>
<tr><td colspan="1">Power</td><td colspan="2">Velocity</td><td colspan="2">P/V ratio</td></tr>
<tr><td colspan="5">Sensor</td></tr>
<tr><td>Area</td><td>Area STD</td><td>Major Axis</td><td>Minor Axis</td><td>Skewness</td></tr>
<tr><td>Eccentricity</td><td>ECT last 5 layers</td><td>Major Axis STD</td><td>Minor Axis STD</td><td>Skewness STD</td></tr>
<tr><td>Eccentricity STD</td><td>ECT STD</td><td colspan="3"></td></tr>
</table>

It was found that for prediction using just the Parameter and Sensor features, all 15 features were needed for a high fidelity classification model. This can be seen in Figure 5-12, where the learning curve shows that as more features are added, the higher the F-Score goes and thus the more accurate the model's prediction.

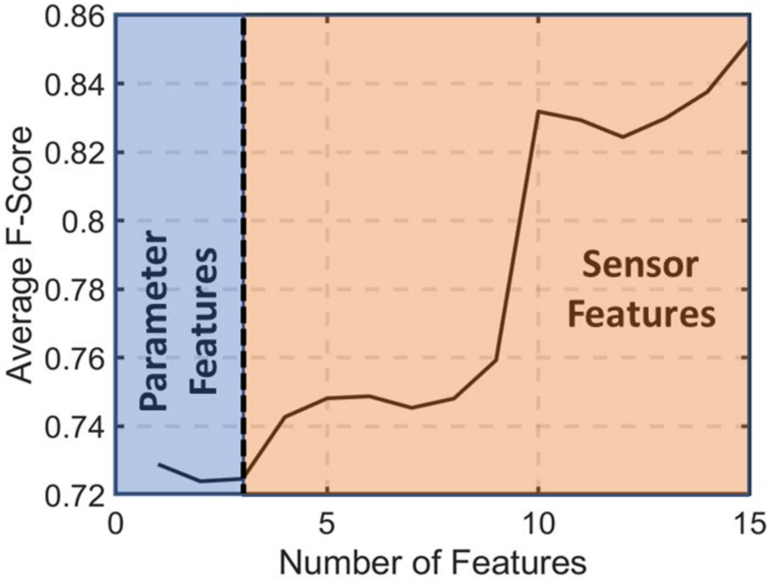

Figure 5-12: Learning curve comparing F-score to the number of features used. The first three features used were the parameters and alone have an F-Score of ~73%. When Sensor Features were added in addition to the parameters there was a jump in accuracy. This accuracy increase continued until all 15 available features were used. All 15 features were needed for high fidelity classification prediction.

For the last category, Parameters + Sensor + Graph Theory, there was a total of twenty-seven features available for use. For feature selection, the method of maximum relevance minimum redundancy (MRMR) was used to determine what features are the most relevant to prediction of meltpool depth. MRMR is an algorithm that is used to assist in the development of feature selection. It is designed to select features that have the highest correlation to the classes and the least correlation to other features. For the feature data sets, MRMR was run 1000 times with randomized data selection from classification data sets and the number of occurrences of each feature in the ranked list was found.

The top 10 features were:

- Power
- Velocity

- P/V ratio
- Meltpool Area
- Meltpool Skewness
- Meltpool Eccentricity
- Standard deviation of Eccentricity
- (n) Full width Half Max
- (n) End-of-Cycle temperature
- (n-2) End-of-Cycle temperature

An evaluation of the Parameters + Sensor's learning curve was performed; this can be seen in Figure 5-13.

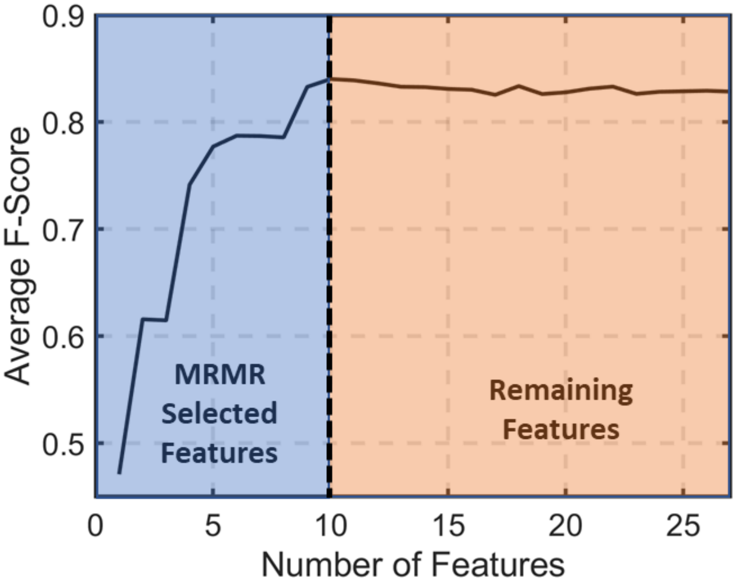

Figure 5-13: Learning curve showing the 10 features determined to be used via minimum redundancy maximum relevance (MRMR) compared to all the features. MRMR's algorithm selected features and numbered them based on their overall relevance to the ground truth. This method also compares feature correlation to each other to reduce the redundancy within the feature set. This can be seen in the removal of the features major and minor axis and not eccentricity. As eccentricity is derived from major and minor axis, it has a high correlation and thus using both in the feature set could be redundant.

5.4 Meltpool Depth Predictions

The meltpool data was split into two data sets, a training set and a testing set. The split of the data was chosen to be 80% training set and 20% testing set. This was chosen as the total number of data points available after the Classification split to reduce bias was 768 data points. This gave 615 data points in the training set and 153 data points in the testing set. There was a loss from balancing the data class split of 439 data points. A total of 100 train-test iterations were performed where the training and testing data were randomized, and the model was re-trained on the new training data. This was to ensure there was no overfitting to a specific subset of the data. The meltpool depth predictions were run on each of the prediction models for each of the three categories. This consisted of 3 steps. These steps are optimization of the model, training of the model, and testing of the model. Optimization found the setting and parameters of the model that would then be applied to the Training step. The default MATLAB Optimization settings were used, and the model setting saved.

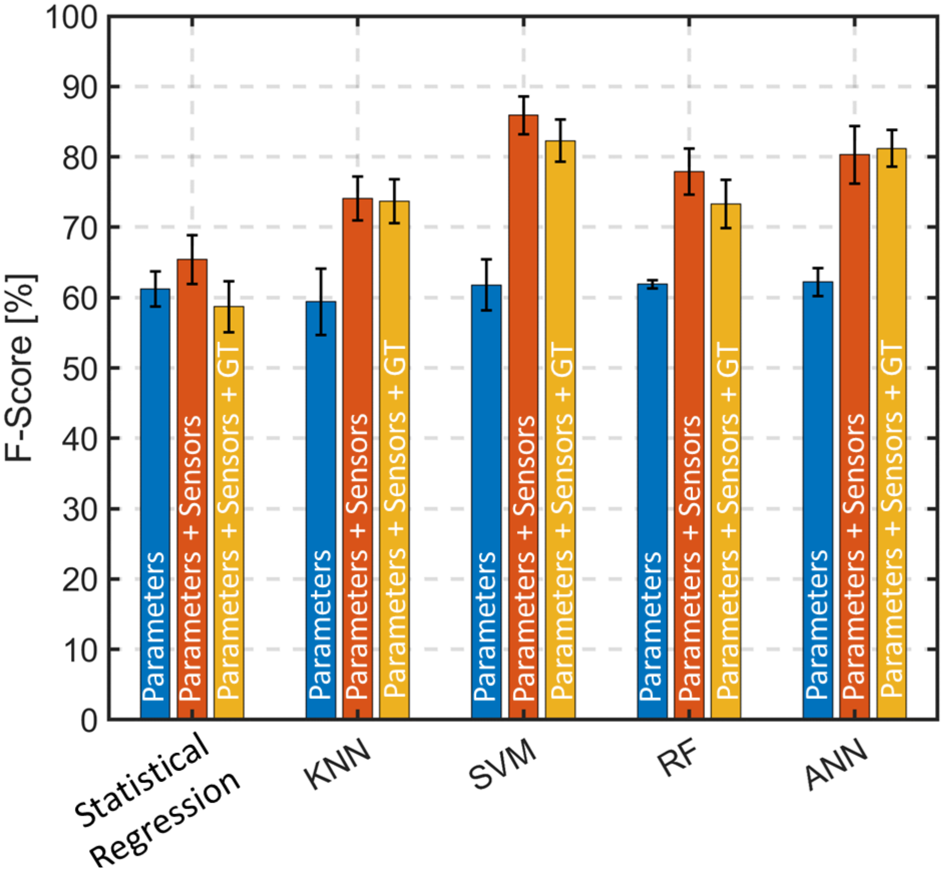

Figure 5-14: Machine learning classification results per model using different numbers of features and types of sensors. This shows that process parameters are not sufficient for prediction of meltpool depth and sensor features are needed for a higher accuracy prediction. Highest accuracy model was SVM at 85.9%.

Each model was run 100 times on the train-test cycle and its outputted performance metrics were recorded; the average and standard deviation of the F-score were found. Figure 5-14 shows the results of these runs for the classification prediction. These results indicate that the highest accuracy model is SVM at 85.9% when using the Parameters + Sensor feature set. The next closest was the ANN at 81.2%, using the feature set Parameters + Sensor + Graph Theory. When exploring these results, the outcome of the Parameters category is of interest. These three features were able to give approximately 60% accuracy across all models.

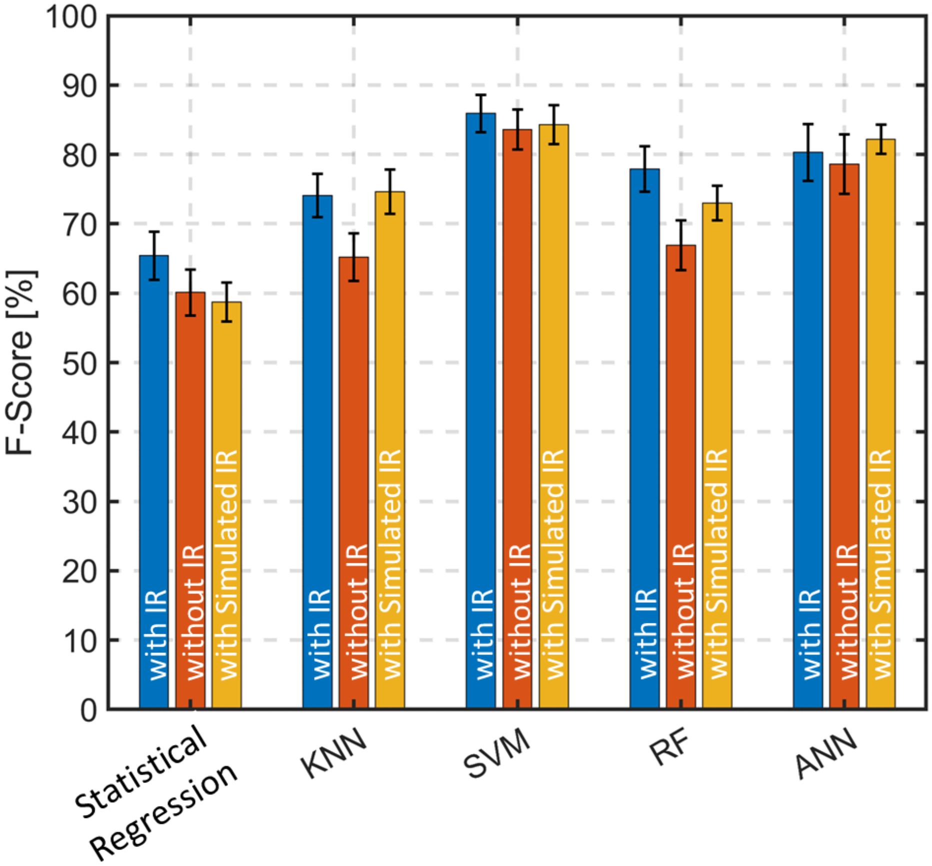

Figure 5-15: Class prediction results with infrared features, without infrared features, and with simulated infrared features. There was approximately a 5%-10% drop in F-Score when the infrared end-of-cycle feature was removed from the feature set. When the thermal date was replaced with simulated infrared features from graph theory simulation the accuracy was restored to similar accuracy values with the real infrared data. Thermal simulations could be used as a replacement for in-situ sensor data.

An analysis on the impact of the infrared end-of-cycle data was done to see its influence on the accuracy of the meltpool depth prediction. These findings are from the same feature set list as the Parameters + Sensor category with the exclusion of the IR features. This reduces the feature set list from 15 features to 13 Features.

Based on this omission of the IR features shown in Figure 5-15, a loss of accuracy of approximately 5% across many of the models can be found. While this is a significant drop in accuracy, the fact that the accuracy only dropped by 5% indicates that the features that were extracted from the meltpool are far more important in the prediction of meltpool depth. Additionally, when end-of-cycle features were put back in the model via the form of graph theory thermal simulation results, the model increased its prediction accuracy again. This indicates the potential for using simulations in place of sensors for the prediction of flaws in LPBF and meltpool depth.

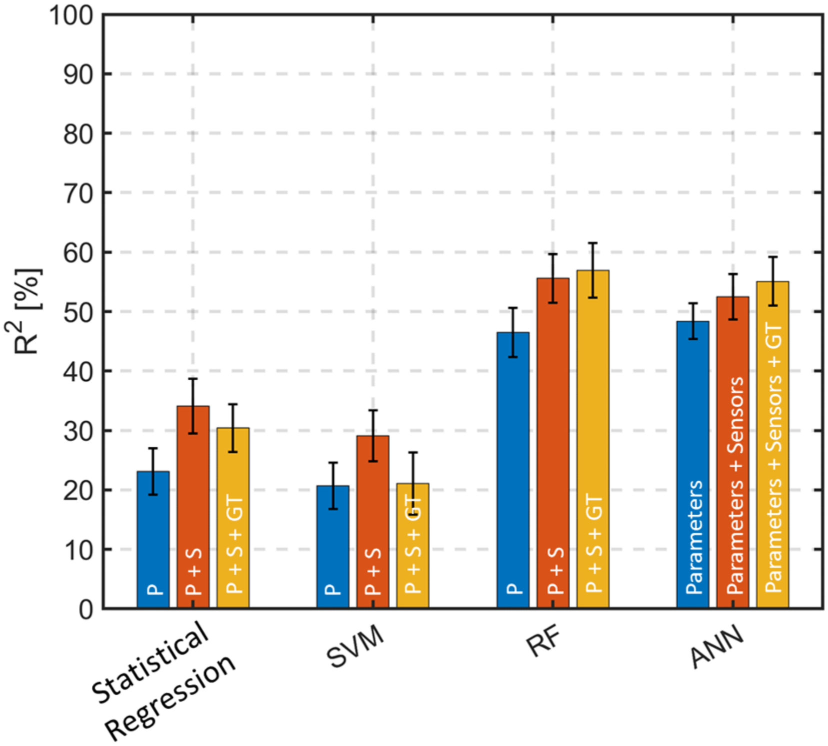

Figure 5-16: Machine learning regression results per model for different numbers of features and sensor types. This shows that the feature set is unsuitable for regression as only the support vector machine (SVM) and the artificial neural network (ANN) were able to reach an accuracy of R^2 = ~50%.

Four models were chosen to explore the feature set's ability to predict meltpool depth using regression prediction. Random Forest and ANN gave comparable results for regression of R^2 values of greater than 50%. With the best model being the Random Forest using the feature set of Parameters + Sensor + Graph Theory, this model gave an R^2 value of 56.9%. The ANN produced results of an R^2 value of 55.1%. These results show (Figure 5-16) that this feature set is unsuitable for regression modeling.

While unsuited for regression prediction of meltpool depth, they do show the same increase in accuracy when meltpool features were added. This supports the notion that while parameters make up a substantial portion of the accuracy found in the models, meltpool features and characteristics make up the details needed for a higher fidelity model.

5.5 Visual Comparison of PDAS

A visual comparison of the primary dendritic arm spacing to the thermal history was done using heatmaps to show regions of larger PDAS or temperature, Figure 5-17. Further use of PDAS is discussed in the Future Works section.

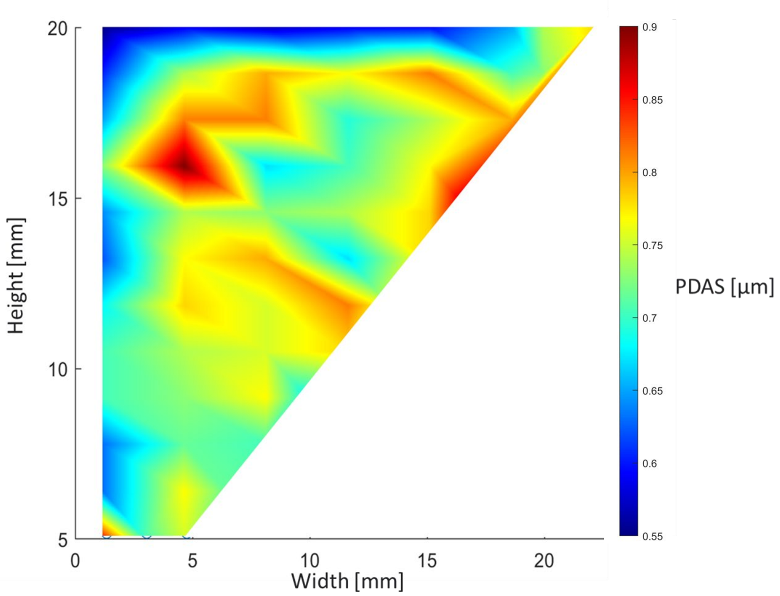

Figure 5-17: Primary dendrite arm spacing (PDAS) size map. There is an increase in PDAS as the height increases. This could be due to the heat accumulation in the overhang. The heat accumulation could give more time for dendrites to form.

The PDAS size map, Figure 5-17, shows an increase in the upper portion of the part. This makes sense as these parts were designed to have heat accumulate in the overhang section. This heat accumulation gives a higher end-of-cycle temperature for the previous layer giving the following heating-cooling cycle a higher end-of-cycle temperature, giving more time for dendrites to form. It is of note that the last layer or top of the part has a lower PDAS than expected. This would be from the fact that the last layer does not receive any reheating cycles to drive the temperature of that area above the eutectic temperature. The previous layers receive heat from the formation of the new layers above them, and as the meltpool depth measurements show, there is an average penetration of 3.11 layers for part 4A. The final layer did not undergo remelting and thus there was no additional time above the eutectic temperature, resulting in a decrease in the scale of the PDAS when compared to the previous layers.

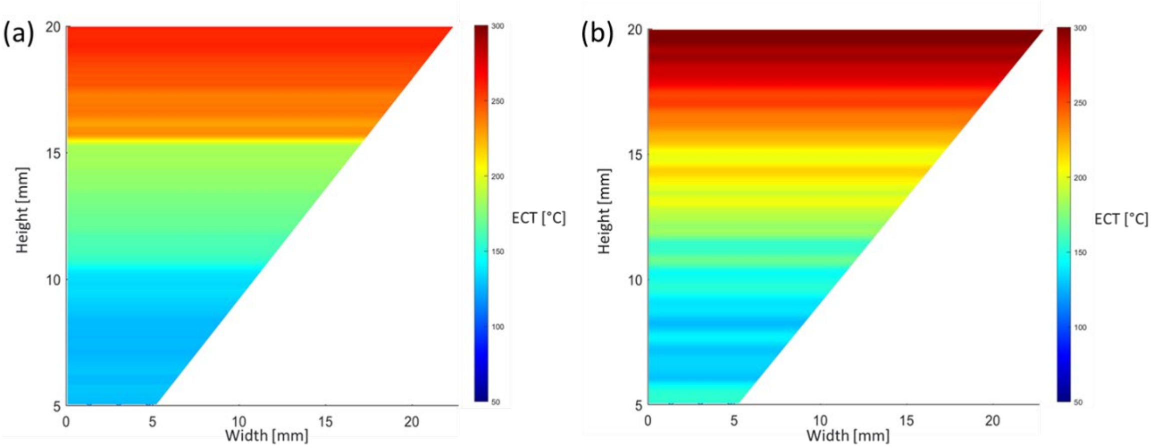

Figure 5-18: (a) The infrared data for end-of-cycle temperature and (b) thermal simulation of end-of-cycle temperature data comparison. The infrared data show clear separation and jumps in the end-of-cycle temperature as the C and then B parts finish. With fewer parts on the build plate there is less time between the layers giving less time for cooling. This and the geometry drive heat accumulation. The infrared data and thermal simulation data show similar results but there is more definition in the layer in the thermal simulation.

The IR data for end-of-cycle temperature shows clear striations and separation from when the C and then B parts finished printing. The thermal simulation shows similar results to the IR data, however there is further definition in the layer than observed in the IR data, shown in Figure 5-18. This could be that the model is more sensitive to the inter layer time, giving a sharper increase in end-of-cycle temperature than was seen at height 10 mm or 15 mm in the IR data.

CHAPTER 6 – CONCLUSIONS AND FUTURE WORK

This work investigated the prediction of meltpool depth in Laser Powder Bed Fusion. Specific contributions from this work are as follows:

1) Designed and built twenty-one Inconel 718 overhangs of three different heights.
2) Collected in-situ data with a dual wavelength pyrometer and an infrared camera.
3) Extracted meltpool characteristics and end-of-cycle temperature from said sensors.
4) Measured meltpool depth using an optical microscope.
5) Correlated sensor data to real world spatial location in the parts.
6) Created feature sets from parameters, extracted sensor data, and graph theory simulations.
7) Selected features from each category to maximize prediction success and accuracy.
8) Implemented optimized feature sets on 5 classification prediction models and 4 regression prediction models.

Analyses of end-of-cycle temperatures, meltpool depth measurements, and meltpool areas were performed. From the IR temperature data, it was found that energy density was not a good predictor of end-of-cycle temperature. As power increased, end-of-cycle temperatures also increased. The meltpool depth measurements showed there was a nonlinear relationship between the power-velocity ratio and this nonlinearity. These discoveries reinforced the decision to use machine learning to predict meltpool depth. The meltpool area showed that as power increased there was an increase in meltpool area. These finding show a relationship between the power, scan speed, meltpool area, and meltpool depth. As the energy density increased past the nominal there was a trend for the heat to dissipate towards melting of the surrounding powder instead of the previous layers, causing the meltpool widen and spill over into the surrounding horizontal directions, giving a larger meltpool area. This widening of the meltpool resulted in reduced meltpool depth.

The following results are quantifiable performance metrics that were used to evaluate the accuracy of the prediction. Meltpool depth was correctly predicted with an F-Score accuracy of 85.9% with a standard deviation of 2.7% using a Support Vector Machines machine learning model. It was found that while the parameter features make up a majority portion contributing to the accuracy found in the models, the meltpool features and characteristics had a larger effect on the meltpool depth prediction and were needed to create a high-fidelity prediction model. It was also found that this feature set was unsuitable for regression prediction.

Furthermore, SEM images were captured, and visualizations were created to aid in the future work of prediction of primary dendritic arm spacing. This work shows locations of higher PDAS and attempts to understand how the thermal effects relate to them.

Flaws in this work could come from calibration of the sensors, this was minimized by taking a calibration to a known actual temperature and correlating this known temperature to IR data. Another source of error could be the correlation of the pyrometer data's frames to spatial location in the part. As both the meltpool depth measurements and the hatch location alignment were done by hand, there could be flaws in this created relation; meltpools could have been missed or skipped at the edges of the picture or part. This error could account for the model's accuracy not reaching above 86%.

The future work of this research would be to expand predictions to primary dendritic arm spacing. For this future work, all features created and outputs predicted (meltpool depth) could be applied as the input feature sets. To do this, the approximately 1,800 SEM images that were collected would need to be evaluated for PDAS and their location within the part.

Using the methodology set out in this thesis, meltpool characteristics could be extracted and segmented throughout the whole volume of the twenty-one parts. Each hatch of each layer could have a meltpool feature set extracted and correlated to its real-world location. PDAS measurements could then be taken and by interpolating between data points, a complete map of the PDAS of the part could be created. From this feature set and ground truth PDAS data, machine learning models could then be evaluated for prediction accuracy of PDAS.

If this experiment were to be re-run there could be additional features extracted from a completely functional pyrometer sensor. This would open avenues of use for initial meltpool temperatures, giving rise to a more complete heating/cooling curve of the part. From this, meltpool temperature and thermal history simulations, the cooling rates, or an approximation of the cooling curve could be evaluated into features. Given the equations for the formation of PDAS, which are based on the cooling rates, features that could have a positive influence on accuracy could be created.

This initial or exploratory work lays out the methodology that is needed to extract useful information from in-process sensor data and thermal simulations and demonstrates that it is possible to predict meltpool depth to a certain degree of accuracy.

The data that supports the findings of this thesis are available by contacting Dr. Prahalada Rao. Restrictions apply due to the data being a part of several ongoing studies and will be made available in due course.

REFERENCES CITED

[1] M. Montazeri and P. Rao, “Sensor-Based Build Condition Monitoring in Laser Powder Bed Fusion Additive Manufacturing Process Using a Spectral Graph Theoretic Approach,” *Journal of Manufacturing Science and Engineering, Transactions of the ASME*, vol. 140, no. 9, Sep. 2018, doi: 10.1115/1.4040264.

[2] F. Imani, A. Gaikwad, M. Montazeri, P. Rao, H. Yang, and E. Reutzel, “Process Mapping and In-Process Monitoring of Porosity in Laser Powder Bed Fusion Using Layerwise Optical Imaging,” *J Manuf Sci Eng*, vol. 140, no. 10, Oct. 2018, doi: 10.1115/1.4040615.

[3] B. Yao, F. Imani, A. S. Sakpal, E. W. Reutzel, and H. Yang, “Multifractal Analysis of Image Profiles for the Characterization and Detection of Defects in Additive Manufacturing,” *J Manuf Sci Eng*, vol. 140, no. 3, Mar. 2018, doi: 10.1115/1.4037891.

[4] W. J. Sames, F. A. List, S. Pannala, R. R. Dehoff, and S. S. Babu, “The metallurgy and processing science of metal additive manufacturing,” *International Materials Reviews*, vol. 61, no. 5, pp. 315–360, Jul. 2016, doi: 10.1080/09506608.2015.1116649.

[5] S. K. Nayak, S. K. Mishra, A. N. Jinoop, C. P. Paul, and K. S. Bindra, “Experimental Studies on Laser Additive Manufacturing of Inconel-625 Structures Using Powder Bed Fusion at 100 μm Layer Thickness,” *J Mater Eng Perform*, vol. 29, no. 11, pp. 7636–7647, Nov. 2020, doi: 10.1007/s11665-020-05215-9.

[6] M. A. Balbaa, M. A. Elbestawi, and J. McIsaac, "An experimental investigation of surface integrity in selective laser melting of Inconel 625," *The International Journal of Advanced Manufacturing Technology*, vol. 104, no. 9–12, pp. 3511–3529, Oct. 2019, doi: 10.1007/s00170-019-03949-y.

[7] X. Y. Fang, H. Q. Li, M. Wang, C. Li, and Y. B. Guo, "Characterization of texture and grain boundary character distributions of selective laser melted Inconel 625 alloy," *Mater Charact*, vol. 143, pp. 182–190, Sep. 2018, doi: 10.1016/j.matchar.2018.02.008.

[8] J. A. Gonzalez, J. Mireles, S. W. Stafford, M. A. Perez, C. A. Terrazas, and R. B. Wicker, "Characterization of Inconel 625 fabricated using powder-bed-based additive manufacturing technologies," *J Mater Process Technol*, vol. 264, pp. 200–210, Feb. 2019, doi: 10.1016/j.jmatprotec.2018.08.031.

[9] W. E. King *et al.*, "Laser powder bed fusion additive manufacturing of metals; physics, computational, and materials challenges," *Appl Phys Rev*, vol. 2, no. 4, p. 041304, Dec. 2015, doi: 10.1063/1.4937809.

[10] C. Zhao *et al.*, "Real-time monitoring of laser powder bed fusion process using high-speed X-ray imaging and diffraction," *Sci Rep*, vol. 7, no. 1, p. 3602, Dec. 2017, doi: 10.1038/s41598-017-03761-2.

[11] K. Gruber, I. Smolina, M. Kasprowicz, and T. Kurzynowski, "Evaluation of Inconel 718 Metallic Powder to Optimize the Reuse of Powder and to Improve the Performance and Sustainability of the Laser Powder Bed Fusion (LPBF) Process," *Materials*, vol. 14, no. 6, p. 1538, Mar. 2021, doi: 10.3390/ma14061538.

[12] R. Hague *, S. Mansour, and N. Saleh, “Material and design considerations for rapid manufacturing,” *Int J Prod Res*, vol. 42, no. 22, pp. 4691–4708, Nov. 2004, doi: 10.1080/00207840410001733940.

[13] MSFC and NASA, “Specification for control and qualification of laser powder bed fusion metallurgical processes,” *MSFC Technical Standard MSFC-SPEC-3717*, 2017.

[14] S. Patel and M. Vlasea, “Melting modes in laser powder bed fusion,” *Materialia (Oxf)*, vol. 9, Mar. 2020, doi: 10.1016/j.mtla.2020.100591.

[15] Z. Hu and S. Mahadevan, “Uncertainty quantification and management in additive manufacturing: current status, needs, and opportunities,” *The International Journal of Advanced Manufacturing Technology*, vol. 93, no. 5–8, pp. 2855–2874, Nov. 2017, doi: 10.1007/s00170-017-0703-5.

[16] M. M. Attallah, R. Jennings, X. Wang, and L. N. Carter, “Additive manufacturing of Ni-based superalloys: The outstanding issues,” *MRS Bulletin*, vol. 41, no. 10. Materials Research Society, pp. 758–764, Oct. 01, 2016. doi: 10.1557/mrs.2016.211.

[17] R. Fabbro, “Melt pool and keyhole behaviour analysis for deep penetration laser welding,” *J Phys D Appl Phys*, vol. 43, no. 44, p. 445501, Nov. 2010, doi: 10.1088/0022-3727/43/44/445501.

[18] Z. Gan *et al.*, “Universal scaling laws of keyhole stability and porosity in 3D printing of metals,” *Nat Commun*, vol. 12, no. 1, p. 2379, Dec. 2021, doi: 10.1038/s41467-021-22704-0.

[19] Y. Fu, A. R. J. Downey, L. Yuan, T. Zhang, A. Pratt, and Y. Balogun, "Machine learning algorithms for defect detection in metal laser-based additive manufacturing: A review," *J Manuf Process*, vol. 75, pp. 693–710, Mar. 2022, doi: 10.1016/j.jmapro.2021.12.061.

[20] L. Meng *et al.*, "Machine Learning in Additive Manufacturing: A Review," *JOM*, vol. 72, no. 6, pp. 2363–2377, Jun. 2020, doi: 10.1007/s11837-020-04155-y.

[21] P. Akbari *et al.*, "MeltpoolNet: Melt pool characteristic prediction in Metal Additive Manufacturing using machine learning," *Addit Manuf*, vol. 55, Jul. 2022, doi: 10.1016/j.addma.2022.102817.

[22] F. L. Vecchiato, H. de Winton, P. A. Hooper, and M. R. Wenman, "Melt pool microstructure and morphology from single exposures in laser powder bed fusion of 316L stainless steel," *Addit Manuf*, vol. 36, Dec. 2020, doi: 10.1016/j.addma.2020.101401.

[23] W. J. Reynolds, "Predicting melt pool behaviour in LPBF through high fidelity modelling," University of Nottingham, 2022.

[24] Q. Guo *et al.*, "In-situ characterization and quantification of melt pool variation under constant input energy density in laser powder bed fusion additive manufacturing process," *Addit Manuf*, vol. 28, pp. 600–609, Aug. 2019, doi: 10.1016/j.addma.2019.04.021.

[25] G. Tapia, S. Khairallah, M. Matthews, W. E. King, and A. Elwany, "Gaussian process-based surrogate modeling framework for process planning in laser powder-bed fusion additive manufacturing of 316L stainless steel," *International Journal of*

Advanced Manufacturing Technology, vol. 94, no. 9–12, pp. 3591–3603, Feb. 2018, doi: 10.1007/s00170-017-1045-z.

[26] A. Gaikwad, B. Giera, G. M. Guss, J. B. Forien, M. J. Matthews, and P. Rao, “Heterogeneous sensing and scientific machine learning for quality assurance in laser powder bed fusion – A single-track study,” *Addit Manuf*, vol. 36, Dec. 2020, doi: 10.1016/j.addma.2020.101659.

[27] A. Gaikwad *et al.*, “Multi phenomena melt pool sensor data fusion for enhanced process monitoring of laser powder bed fusion additive manufacturing,” *Mater Des*, vol. 221, Sep. 2022, doi: 10.1016/j.matdes.2022.110919.

[28] M. Grasso and B. M. Colosimo, “Process defects and in situ monitoring methods in metal powder bed fusion: A review,” *Measurement Science and Technology*, vol. 28, no. 4. Institute of Physics Publishing, Apr. 01, 2017. doi: 10.1088/1361-6501/aa5c4f.

[29] G. Tapia and A. Elwany, “A Review on Process Monitoring and Control in Metal-Based Additive Manufacturing,” *J Manuf Sci Eng*, vol. 136, no. 6, Dec. 2014, doi: 10.1115/1.4028540.

[30] S. K. Everton, M. Hirsch, P. Stravroulakis, R. K. Leach, and A. T. Clare, “Review of in-situ process monitoring and in-situ metrology for metal additive manufacturing,” *Mater Des*, vol. 95, pp. 431–445, Apr. 2016, doi: 10.1016/j.matdes.2016.01.099.

[31] M. Mani, B. Lane, A. Donmez, S. Feng, S. Moylan, and R. Fesperman, “Measurement Science Needs for Real-time Control of Additive Manufacturing

Powder Bed Fusion Processes," Gaithersburg, MD, Feb. 2015. doi: 10.6028/NIST.IR.8036.

[32] C. Gobert, E. W. Reutzel, J. Petrich, A. R. Nassar, and S. Phoha, "Application of supervised machine learning for defect detection during metallic powder bed fusion additive manufacturing using high resolution imaging.," *Addit Manuf*, vol. 21, pp. 517–528, May 2018, doi: 10.1016/j.addma.2018.04.005.

[33] P. Mercelis and J. Kruth, "Residual stresses in selective laser sintering and selective laser melting," *Rapid Prototyp J*, vol. 12, no. 5, pp. 254–265, Oct. 2006, doi: 10.1108/13552540610707013.

[34] M. F. Zäh and S. Lutzmann, "Modelling and simulation of electron beam melting," *Production Engineering*, vol. 4, no. 1, pp. 15–23, Feb. 2010, doi: 10.1007/s11740-009-0197-6.

[35] B. K. Foster, E. W. Reutzel, A. R. Nassar, B. T. Hall, S. W. Brown, and C. J. Dickman, "Optical, layerwise monitoring of powder bed fusion," in *2014 International Solid Freeform Fabrication Symposium*, 2015.

[36] F. Bayle and M. Doubenskaia, "Selective laser melting process monitoring with high speed infra-red camera and pyrometer," in *Fundamentals of laser assisted micro- and nanotechnologies*, 2008, vol. 6985, pp. 39–46.

[37] T. Craeghs, F. Bechmann, S. Berumen, and J.-P. Kruth, "Feedback control of Layerwise Laser Melting using optical sensors," *Phys Procedia*, vol. 5, pp. 505–514, 2010, doi: 10.1016/j.phpro.2010.08.078.

[38] T. Craeghs, S. Clijsters, Jean.-P. Kruth, F. Bechmann, and Marie.-C. Ebert, "Detection of Process Failures in Layerwise Laser Melting with Optical Process Monitoring," *Phys Procedia*, vol. 39, pp. 753–759, 2012, doi: 10.1016/j.phpro.2012.10.097.

[39] A. Riensche *et al.*, "Feedforward Control of Thermal History in Laser Powder Bed Fusion: Toward Physics-based Optimization of Processing Parameters," *Mater Des*, p. 111351, Nov. 2022, doi: 10.1016/j.matdes.2022.111351.

[40] Q. Wang, P. Michaleris, M. Pantano, C. Li, Y. Ren, and A. R. Nassar, "Part-scale thermal evolution and post-process distortion of Inconel-718 builds fabricated by laser powder bed fusion," *J Manuf Process*, vol. 81, pp. 865–880, Sep. 2022, doi: 10.1016/j.jmapro.2022.07.026.

[41] R. Yavari *et al.*, "Thermal modeling in metal additive manufacturing using graph theory – Application to laser powder bed fusion of a large volume impeller," *Addit Manuf*, vol. 41, p. 101956, May 2021, doi: 10.1016/j.addma.2021.101956.

[42] E. Rodriguez, J. Mireles, C. A. Terrazas, D. Espalin, M. A. Perez, and R. B. Wicker, "Approximation of absolute surface temperature measurements of powder bed fusion additive manufacturing technology using in situ infrared thermography," *Addit Manuf*, vol. 5, pp. 31–39, Jan. 2015, doi: 10.1016/j.addma.2014.12.001.

[43] R. J. Williams *et al.*, "In situ thermography for laser powder bed fusion: Effects of layer temperature on porosity, microstructure and mechanical properties," *Addit Manuf*, vol. 30, p. 100880, Dec. 2019, doi: 10.1016/j.addma.2019.100880.

[44] P. A. Hooper, “Melt pool temperature and cooling rates in laser powder bed fusion,” *Addit Manuf*, vol. 22, pp. 548–559, Aug. 2018, doi: 10.1016/j.addma.2018.05.032.

[45] B. Lane and H. Yeung, “Process Monitoring Dataset from the Additive Manufacturing Metrology Testbed (AMMT): Overhang Part X4,” *J Res Natl Inst Stand Technol*, vol. 125, p. 125027, Sep. 2020, doi: 10.6028/jres.125.027.

[46] K. D. Cole, M. R. Yavari, and P. K. Rao, “Computational heat transfer with spectral graph theory: Quantitative verification,” *International Journal of Thermal Sciences*, vol. 153, p. 106383, Jul. 2020, doi: 10.1016/j.ijthermalsci.2020.106383.

[47] M. R. Yavari, K. D. Cole, and P. K. Rao, “Design Rules for Additive Manufacturing – Understanding the Fundamental Thermal Phenomena to Reduce Scrap,” *Procedia Manuf*, vol. 33, pp. 375–382, 2019, doi: 10.1016/j.promfg.2019.04.046.

[48] R. Yavari *et al.*, “Part-scale thermal simulation of laser powder bed fusion using graph theory: Effect of thermal history on porosity, microstructure evolution, and recoater crash,” *Mater Des*, vol. 204, p. 109685, Jun. 2021, doi: 10.1016/j.matdes.2021.109685.

[49] A. Riensche *et al.*, “Feedforward Control of Thermal History for Physics-based Optimization of Processing Parameters in Laser Powder Bed Fusion Additive Manufacturing,” *(in press)*.

[50] S. B. Kotsiantis, I. D. Zaharakis, and P. E. Pintelas, “Machine learning: a review of classification and combining techniques,” *Artif Intell Rev*, vol. 26, no. 3, pp. 159–190, Nov. 2006, doi: 10.1007/s10462-007-9052-3.

[51] D. Maulud and A. M. Abdulazeez, “A review on linear regression comprehensive in machine learning,” *Journal of Applied Science and Technology Trends*, vol. 1, no. 4, pp. 140–147, 2020.

[52] N. Matloff, *Statistical Regression and Classification*. Chapman and Hall/CRC, 2017. doi: 10.1201/9781315119588.

[53] Z. Smoqi *et al.*, “Monitoring and prediction of porosity in laser powder bed fusion using physics-informed meltpool signatures and machine learning,” *J Mater Process Technol*, vol. 304, p. 117550, Jun. 2022, doi: 10.1016/j.jmatprotec.2022.117550.

[54] S. Liu, A. P. Stebner, B. B. Kappes, and X. Zhang, “Machine learning for knowledge transfer across multiple metals additive manufacturing printers,” *Addit Manuf*, vol. 39, p. 101877, Mar. 2021, doi: 10.1016/j.addma.2021.101877.

[55] P. Vidyullatha and D. R. Rao, “Machine learning techniques on multidimensional curve fitting data based on R-square and chi-square methods,” *International Journal of Electrical and Computer Engineering*, vol. 6, no. 3, p. 974, 2016.

[56] M. S. Joshi, A. Flood, T. Sparks, and F. W. Liou, “Applications of Supervised Machine Learning Algorithms in Additive Manufacturing: A Review,” in *2019 International Solid Freeform Fabrication Symposium*, 2019.

[57] M. W. Gardner and S. R. Dorling, “Artificial neural networks (the multilayer perceptron)—a review of applications in the atmospheric sciences,” *Atmos Environ*, vol. 32, no. 14–15, pp. 2627–2636, Aug. 1998, doi: 10.1016/S1352-2310(97)00447-0.

This M.S. thesis was funded by the National Science Foundation (NSF) via the following grants:

OIA-1929172

CMMI-1752069

ECCS-2020246

PFI-TT 2044710

CMMI-1920245

CAREER: Smart Additive Manufacturing - Fundamental Research in Sensing, Data Science, and Modeling Toward Zero Part Defects.